



HAL
open science

Facet-Dependent Strain Determination in Electrochemically Synthesized Platinum Model Catalytic Nanoparticles

Jérôme Carnis, Lu Gao, Sara Fernández, Gilbert Chahine, Tobias U Schüllli,
Stéphane Labat, Emiel Hensen, Olivier Thomas, Jan P Hofmann,
Marie-ingrid Richard

► **To cite this version:**

Jérôme Carnis, Lu Gao, Sara Fernández, Gilbert Chahine, Tobias U Schüllli, et al.. Facet-Dependent Strain Determination in Electrochemically Synthesized Platinum Model Catalytic Nanoparticles. *Small*, 2021, 17 (18), pp.2007702. 10.1002/sml.202007702 . hal-03275273

HAL Id: hal-03275273

<https://hal.science/hal-03275273>

Submitted on 24 Jun 2022

HAL is a multi-disciplinary open access archive for the deposit and dissemination of scientific research documents, whether they are published or not. The documents may come from teaching and research institutions in France or abroad, or from public or private research centers.

L'archive ouverte pluridisciplinaire **HAL**, est destinée au dépôt et à la diffusion de documents scientifiques de niveau recherche, publiés ou non, émanant des établissements d'enseignement et de recherche français ou étrangers, des laboratoires publics ou privés.

Facet-dependent strain determination in electrochemically synthesized platinum model catalytic nanoparticles.

Jérôme Carnis, Lu Gao, Sara Fernández, Gilbert Chahine, Tobias U. Schüllli, Stéphane Labat, Emiel Hensen, Olivier Thomas, Jan P. Hofmann, and Marie-Ingrid Richard*.*

Dr. J. Carnis, Dr. S. Fernández, Dr. S. Labat, Prof. O. Thomas, Dr. M.-I. Richard
Aix Marseille Université, CNRS, Université de Toulon, IM2NP UMR 7334
13397 Marseille, France.
E-mail: jerome.carnis@desy.de

Dr. J. Carnis, Dr. S. Fernández, Dr. T. Schüllli, Dr. M.-I. Richard
ID01/ESRF, The European Synchrotron
CS 40220, F-38043 Grenoble Cedex 9, France.
Email: mrichard@esrf.fr

Dr. L. Gao, Prof. E. Hensen, Prof. J. P. Hofmann
Laboratory of Inorganic Materials and Catalysis, Department of Chemical Engineering and
Chemistry, Eindhoven University of Technology
P. O. Box 513, 5600MB Eindhoven, The Netherlands.

Dr. G. Chahine
Univ. Grenoble Alpes, CNRS, Grenoble INP, SIMaP
38000 Grenoble, France

Prof. J. P. Hofmann
Surface Science Laboratory, Department of Materials and Earth Sciences, Technical
University of Darmstadt
Otto-Berndt-Strasse 3, 64287 Darmstadt, Germany.

Dr. M.-I. Richard
Univ. Grenoble Alpes, CEA Grenoble, IRIG, MEM, NRS
17 rue des Martyrs 38000 Grenoble, France

Studying model nanoparticles is one approach to better understand the structural evolution of a catalyst during reactions. These nanoparticles feature well-defined faceting, offering the possibility to extract structural information as a function of facet orientation and compare it to theoretical simulations. Using Bragg Coherent X-ray Diffraction Imaging, we study the uniformity of electrochemically synthesized model catalysts, here high-index faceted tetrahedral platinum nanoparticles at ambient conditions. We obtain three-dimensional images of an individual nanoparticle, assessing not only its shape but also the specific components of the displacement and strain fields both at the surface of the nanocrystal and

inside. Our study reveals structural diversity of shapes and defects, and shows that the tetrahedral platinum nanoparticles present strain build-up close to facets and edges. We further apply a facet recognition algorithm to the imaged nanoparticles and provide facet-dependent structural information for all measured nanoparticles. In the context of strain engineering for model catalysts, this study provides insight into the shape-controlled synthesis of platinum nanoparticles with high-index facets.

1. Introduction

Metal nanoparticles are commonly used in catalysis due to their high surface-to-volume ratio and high surface energy, which make their surface atoms very active. In addition to their superior activity, metal nanoparticles are usually isolable, dispersible and reusable catalysts and, thus, meet some requirements of the modern concept of 'green catalysis'.^[1] A challenging issue in the synthesis of metal nanoparticles is obtaining reproducibly a uniform size, shape and composition, as catalytic activity of metal nanoparticles depends on surface crystallographic and electronic structures. The use of well-defined metal nanoparticle catalysts enables to assess the nature of active sites in the catalytic reaction, which is vital for the rational design of catalysts. Since there is a strong correlation between size, shape, and structure (heterogeneities, defects, *etc.*) of nanoparticles and their properties, the emphasis during synthesis is on the precise control of these structural parameters. Recent progress in fabrication techniques has enabled the synthesis of metal nanoparticles with precisely controlled size, shape and composition. The pioneering work of Tian *et al.* has resulted in the controlled electrochemical syntheses of regularly shaped platinum (Pt) particles^[2] as well as alloys of platinum group metals (PGMs) with high-index facets.^[3] In the case of Pt nanoparticles, it has been shown that high-order facets are beneficial to the catalytic activity: in contrast to close-packed low-index faceted single crystals, nanoparticles with atomically open (high-index) surfaces can be more active for some reactions.^[4] Recently, Pt tetrahedral (THH) nanoparticles have been

analyzed by transmission electron microscopy (TEM) by Tian *et al.*^[2,5] who determined the facets of the particles and proved the high stability of {210} and {310} planes under electrochemical conditions. It has also been demonstrated that high-index facets ensure a higher chemical reactivity of catalysts, because of their high density of atomic steps, edges and kinks, which serve as active sites for breaking and making of chemical bonds.^[6,7]

Probing the three-dimensional (3D) structure of metallic particles and mastering the control of surfaces and interfaces as well as their stability and structural changes at small dimensions (typically several nm) is a real challenge, which calls for a fundamental understanding of the interplay between shape, size, strain, faceting, composition and defects at the nanoscale. Despite the great successes so far, there are still challenges in correlating the structure of nanomaterials with their catalytic properties. In particular, control of the surface structure and the distribution of strain and defects remains extremely difficult.^[8] X-ray diffraction measurements of strain have already been performed on ensembles of metallic particles such as Cu or Pd,^[9] but working at the single particle level is also important for understanding the behavior of ensembles because of unavoidable dispersion.

Bragg coherent X-ray diffraction imaging (BCDI) is a rather new technique successfully used to study the structure of individual nanoparticles. This lens-less technique is based on the measurement of the far field diffraction pattern of an isolated crystalline object illuminated by coherent X-rays and relies on digital methods to replace X-ray imaging lenses. A variety of phase retrieval algorithms are applied to obtain a reconstruction of the object in direct space.^[10,11] It enables the determination of the morphology of particles with a resolution in the range of ~ 10 nm.^[12] When applied under Bragg conditions, CDI has a unique sensitivity to atomic displacements and to the strain distribution. For example, a resolution of 6 nm as well as an atomic displacement accuracy of a few picometers has been reached, while reconstructing

the strain field inside GaN nanostructures containing defects.^[13] Such sensitivity to displacements of the atoms from their equilibrium position means that even the tiny contribution of chemically induced strain (like a change in surface stress) due to adsorption of a monolayer of organic molecules on metal particles can be visualized.^[14] In the case of metallic alloys, it also been shown how the surface strain is sensitive to chemical compositions and can be related to surface reactivities.^[15]

Here, we report BCDI measurements of electrochemically prepared, individual isolated Pt THH nanoparticles supported on polished glassy carbon substrates under ambient conditions. The reconstruction of the 3D diffraction patterns makes it possible to recover the inhomogeneous out-of-plane strain field ε_{zz} inside individual Pt NPs and to determine how it relates to faceting. High-index facets are identified by measuring **002** or **111** Pt streaked Bragg reflections of particles with a size in the range from ~ 200 nm to ~ 400 nm. Automated facet segmentation applied to the phase retrieval output allows the analysis of the retrieved strain depending on various criteria such as the facet or facet family. The main interest of this approach is to provide more accurate experimental data for later comparison with density-functional theory or more coarse-grained simulations of crystal shape and strain by force field methods.

2. Results and discussion

A typical sample consists of crystalline Pt nanoparticles randomly oriented on a glassy carbon substrate (see **Figure 1**). The electrodeposition process induces the formation of 24 $\{hk0\}$ facets leading to the characteristic THH shape of the Pt nanoparticles, as reported by Zhu *et al.*^[16] The THH shape can be described as a cube whose faces are capped by square-based pyramids.

BCDI was used to investigate the structure of single isolated Pt nanoparticles at room temperature and at atmospheric pressure at ID01 beamline of the European synchrotron

(ESRF).^[17] A schematic overview of the experimental set-up is displayed in Figure 1 and described in more detail in Ref.^[18] The intensity distribution around the **002** or **111** Pt reflection was measured in vertical scattering geometry at an X-ray energy of 9 keV.

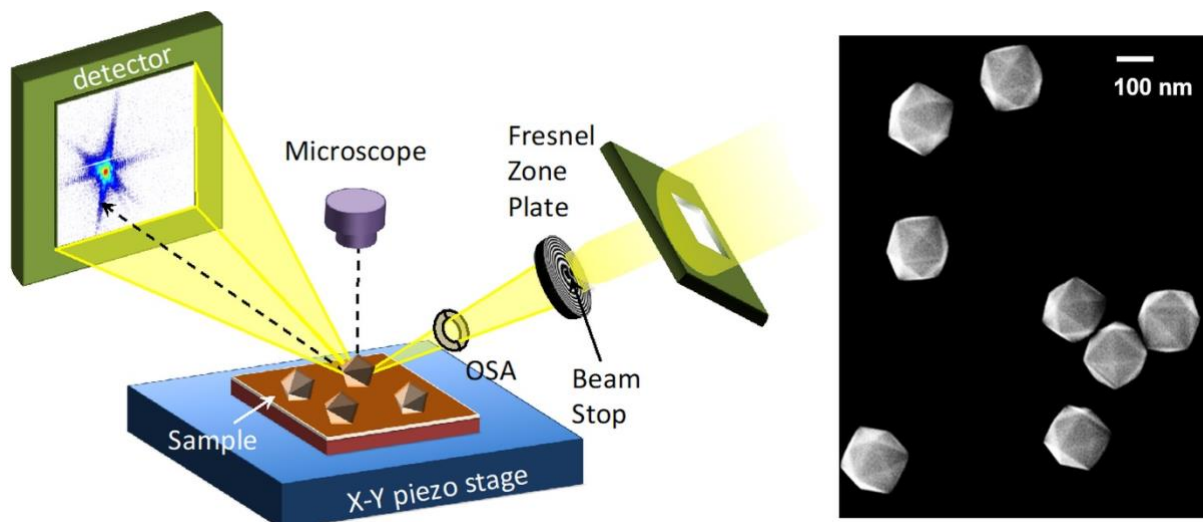


Figure 1. (Left) Scheme of the experimental setup in co-planar diffraction geometry. A microscope is positioned above the sample. The incoming X-ray beam is focused using a Fresnel zone plate. The order-sorting aperture blocks higher diffraction orders. (Right) Scanning electron microscopy image of THH nanoparticles.

As the orientation of the particles on the substrate is random, the intensity distribution of the **002** or **111** Pt Bragg reflection was mapped out on a large area of the substrate surface using the quickK-mapping method developed at the ID01 beamline.^[19] Scanning the substrate in this way, several (001) or (111)-oriented Pt nanoparticles were localized and then measured individually in the focused X-ray beam. Once a particle was illuminated, a 3D reciprocal space map was recorded by performing a rocking-scan across the Bragg angle: the scattering angle was fixed, while the sample was rotated over a few degrees with respect to the direction of the incoming beam. In the following, we consider the frame of reference where x is downstream, y outboard and z vertical up. **Figure 2** displays the sum of the measured intensity along the y and z components of the scattering vector Q for six different single isolated Pt NPs, after interpolating the diffraction data onto an orthonormal grid (labels from 1 to 6 will be used

throughout this manuscript). Apart from a simple in-plane rotation of the NP, differences between diffraction patterns measured at the same reflection can arise from shape variation but also from different internal strain fields. Most of the diffraction patterns show well-defined streaks arising from facets or planar defects. The diffraction pattern corresponding to particle 1 is almost perfectly centrosymmetric, which is the indication of a defect-free nanoparticle. Particle 4 shows an intense streak, which is the sign of a flat interface, probably due to crystal twinning. Defects in the nanocrystal lead to destructive interference effects, which can strongly affect the individual diffraction pattern.^[20] Particle 6 shows broad streaks which arise from small facets, and the larger spacing between fringes indicates that the particle is smaller than particle 5, since both were measured at the same sample-to-detector distance.

The center of mass of the Bragg peak corresponds to the average lattice constant of the single Pt particles. The average Bragg position is obtained by computing the center of mass (COM) of the Bragg peak. For particles 1 to 6, the average lattice constant is 3.9306 Å, 3.9309 Å, 3.9322 Å, 3.9326 Å, 3.9253 Å and 3.9269 Å respectively (lattice constant values +/- 0.0004 Å, taking into account the uncertainty in energy of +/- 1 eV at 9 keV, the nanoparticle being ideally at the center of rotation of the goniometer for the BCDI measurement). Compared to the bulk lattice parameter of Pt of 3.9242 Å,^[21] this yields an average out-of-plane strain $\langle \epsilon_{zz} \rangle = (d_{meas} - d_{ref}) \div d_{ref} \sim 0.14\% \pm 0.01\%$, (d_{meas} and d_{ref} being the measured and theoretical d -spacing) and consequently the majority of the particle volume is relaxed to the intrinsic cubic Pt lattice constant. The observed asymmetry of scattering patterns is thus likely to originate from surface-related effects and/or strain heterogeneities in the particles.

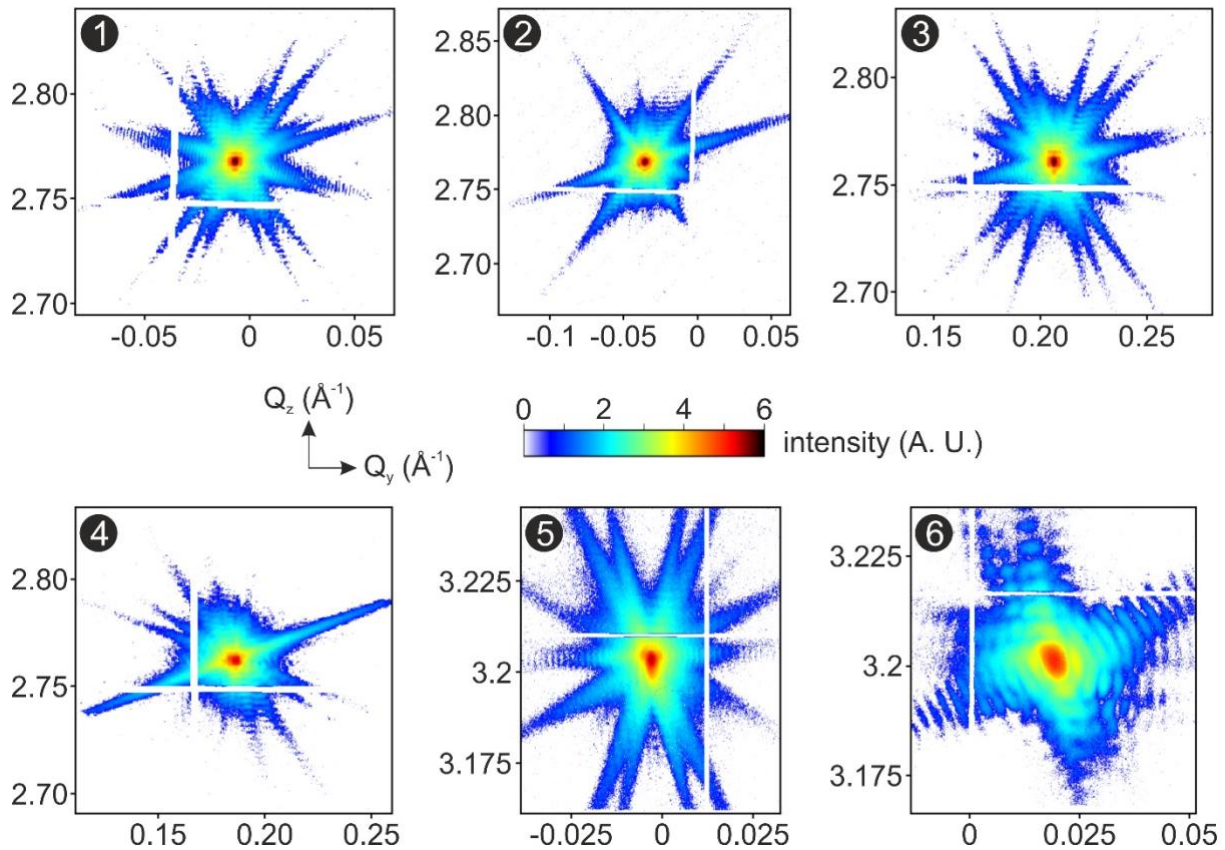


Figure 2. Sum of the measured intensity (logarithmic scale) displayed as a function of the Q_y and Q_z reciprocal space coordinates, for six different isolated THH Pt nanoparticles. Particles 1 to 4 were measured at **111** Pt reflection and at a sample to detector distance of ~ 0.50 m; particles 5 and 6 were measured at **002** Pt reflection and at a sample to detector distance of ~ 1.26 m. An intensity threshold of 1 photon was applied for easier visualization.

Phase retrieval was applied to the six diffraction patterns of Figure 2. The resolution of the reconstruction was estimated using the spherically averaged phase retrieval transfer function (PRTF) ^[22] and ranges from ~ 16 nm to ~ 38 nm. The procedure for phase retrieval is detailed in Methods, and the PRTF are available in the supporting information. Nanoparticle 1 is an example of a perfect THH shape. Note that for this experiment the THH particles were grown onto a glassy carbon substrate. The growth of the area in contact with the substrate was prohibited, resulting in a hole as can be seen in Figure S1 left. The reconstructed modulus is related but not directly proportional to the electron density, and is often called the Bragg electron density for distinction.^[23] Regions around crystalline defects appear as holes in the

reconstructed modulus, as illustrated by a dislocation core in nanocrystal 4 (see **Figure 3** and the supporting information for different views). Another common defect impacting the reconstructed modulus is twinning, where one part of the crystal being measured has a different crystallographic orientation and therefore diffracts in another region of reciprocal space. Nanocrystals 4 and 5 of Figure 3 are examples of missing regions in the reconstructed modulus due to twinning. The reconstructed $\{111\}$ twin boundary for nanocrystal 4 is in agreement with the $\langle 111 \rangle$ streak observed in the 3D diffraction pattern displayed in Figure 2. $\Sigma 3\{111\}$ twin boundaries are commonly observed in face-centered cubic structure,^[24,25] for low stacking-fault energy metals like Ag or Cu. This is more surprising for Pt where the stacking-fault energy is rather high.^[26] Twinning is rarely observed in Pt bulk crystals, however it has already been observed in nanocrystals.^[27] The formation of a twin boundary is a probable final configuration of coalesced nanoparticles, even if the material shows high stacking-fault energies.^[28] This may explain the occurrence of twin boundaries in the studied nanocrystals, which is supported by scanning electron microscopy measurements (see Figure S2). Nanocrystals 2 and 6 display regions on one side where the growth stopped, resulting in a rough surface.

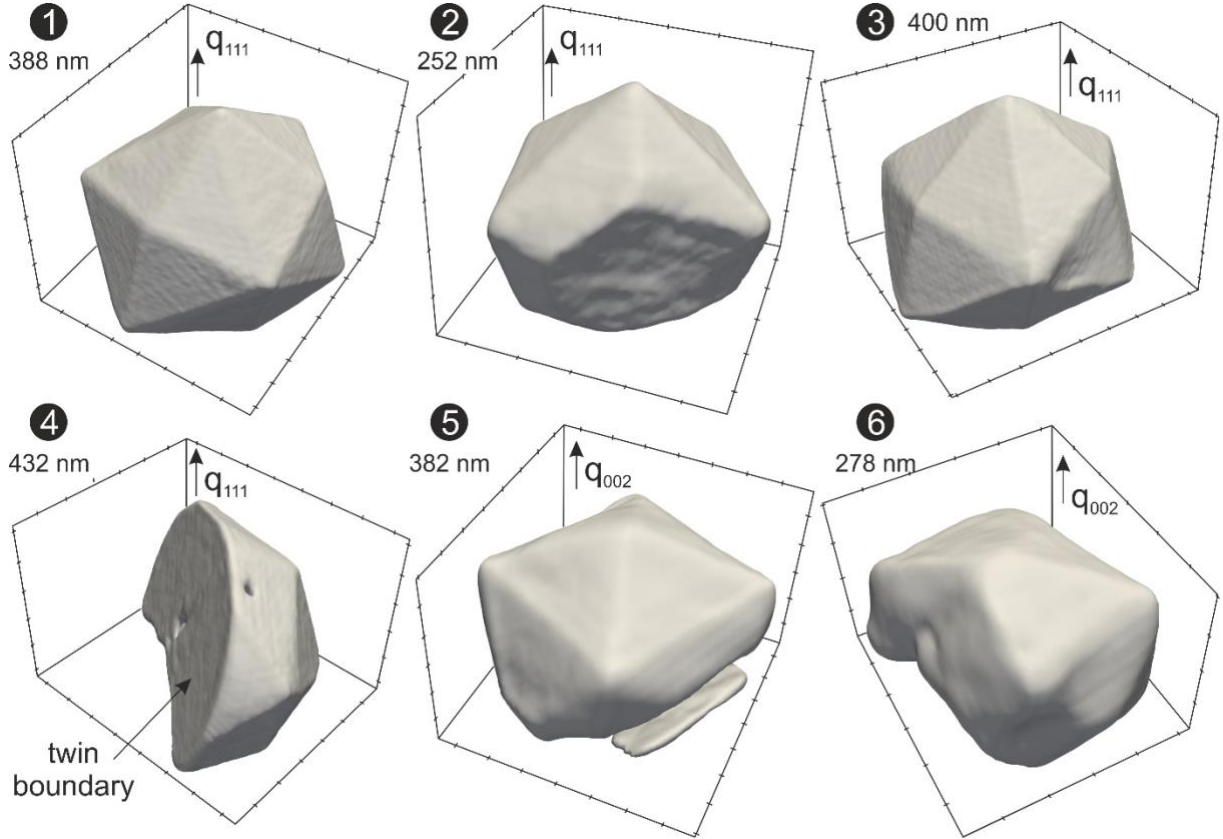


Figure 3. Isosurface views of the Bragg electron density of the six different THH nanoparticles reconstructed by phase retrieval. The isosurface is determined by a threshold on the reconstructed normalized modulus: 0.38, 0.48, 0.48, 0.48, 0.35 and 0.25, respectively. The measurement direction has been aligned with the vertical axis of the reconstructed volume. Tick spacing represents 50 nm. The largest lateral size at mid-height for each nanoparticle is indicated next to its label.

The phase φ obtained by phase retrieval is related to the displacement of lattice points compared to the perfect lattice by the formula $\varphi(\mathbf{r}) = -\mathbf{G}_{hkl} \cdot \mathbf{u}(\mathbf{r}) + \varphi_0$.^[29] For convenience, \mathbf{G}_{hkl} was aligned after phase retrieval along the vertical axis z of the reference frame, so that $\varphi(\mathbf{r}) = -\|\mathbf{G}_{hkl}\| \cdot u_z(\mathbf{r}) + \varphi_0$. The unknown offset φ_0 is often chosen such that the phase is null at the center of mass of the reconstructed modulus. It is therefore important to understand the reconstructed displacement as a displacement relative to the origin of phases. The strain component ε_{zz} is obtained as the gradient of the displacement along the measurement direction and is therefore not affected by the phase offset. Views of the surface displacement and strain,

as well as slices through the reconstructed volume, are available in the supporting information. As the gradient of the displacement, the strain is very sensitive to experimental noise and artefacts related to the use of fast Fourier transforms in the phase retrieval algorithms.^[30] Methods such as phase averaging or apodization exist to reduce noise or artefacts, but in this work we choose a statistical approach relying on the large number of reconstructed voxels (see below).

As a first example, one can group the voxels depending on whether they belong to the surface voxel layer or to the rest of the reconstructed nanocrystal (named the bulk hereafter). The definition of the surface is ambiguous in BCDI because it relies on the numerical choice of a threshold on the reconstructed modulus. Only recently an attempt has been made to define a criterion based on the histogram of the modulus,^[30] which is also used in this work (see Methods). Note that the surface layer will have a thickness corresponding to the voxel size, typically in the few nanometers. However, the extracted strain values have to be understood in the context of the obtained resolution, often corresponding to several voxels. Nevertheless, this simple segmentation provides some insight when comparing the histograms of retrieved strain, as shown in **Figure 4**. For all nanocrystals, the distribution of strain at the surface voxel layer spreads over a larger range than for the bulk, indicating larger strain dispersion at the nanoparticle surface compared to the bulk. Except for nanocrystal 2, the surface strain distribution is also slightly negative (corresponding to compressive out-of-plane strain). The surface of nanoparticles is expected to be in compression due to the lower coordination of lattice sites near the surface.^[31] However, since we measured only the component ε_{zz} of the strain tensor, we cannot draw conclusions at this stage.

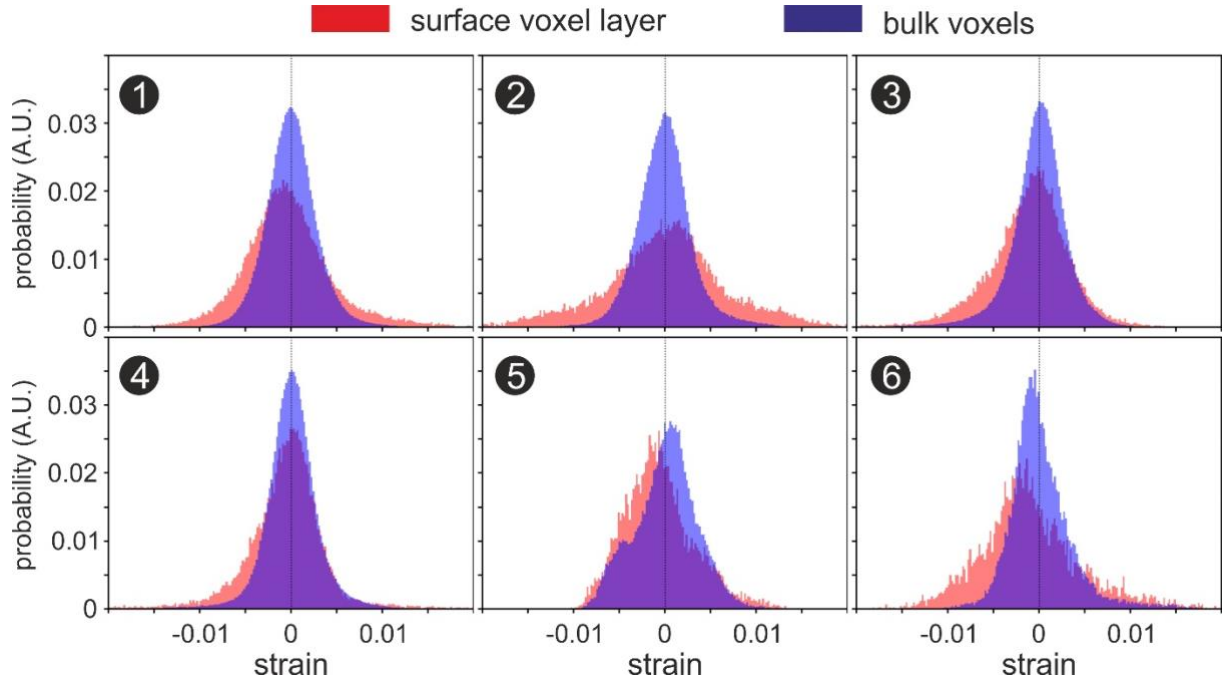


Figure 4. Probability density function of the out-of-plane strain component ε_{zz} for the six nanoparticles, plotted for the surface voxel layer defined by the isosurface threshold (outer layer of the nanoparticle reconstructed by phase retrieval) and the rest of the reconstructed voxel (bulk of the nanoparticle, the surface voxels being excluded). The vertical dashed line is a guide for the eyes and indicates the position of zero strain. The strain histograms were normalized by the number of voxels in the corresponding object (surface or bulk, respectively).

There are a few issues with this approach based on histograms. First of all, the surface layer is defined by a threshold on the reconstructed modulus, which means that twin boundaries (nanoparticles 4 and 5) but also parts with a lower modulus inside the crystal (such as the dislocation core in nanoparticle 4) will be included. Another issue of this histogram approach is that the relationship between the nanoparticle structure/shape/faceting and the local strain information is lost. Since our model nanocrystals are well-faceted despite eventual defects, it is interesting to analyze the strain by facets or $\{hkl\}$ family of facets. Theoretical models and density-functional theory simulations of facet crystallographic planes could then be compared directly with the experiment. Following the work of Grothausmann *et al.*,^[32] we developed an automated three-dimensional python-based facet recognition algorithm.^[33] The workflow of the algorithm is displayed in **Figure 5**. A detailed explanation of the different steps is provided in Methods. The algorithm allows detecting a crystal's facet using the density of normals of each

triangle of the surface mesh of the reconstruction. The surface normals point towards the same direction in case of a facet; therefore the local density of surface normals is large at that point. In contrary, if the surface is very rough, normals point in different directions and the density is small (see Figures 5(c)-(d)). It is advantageous at this stage to project the 3D density of surface normals using a stereographic projection,^[34] because this projection can already provide some information about the type of facets and the symmetry of the nanoparticle. There are two projections, one from the South Pole and the other one from the North Pole, corresponding to facets whose normal has a positive or negative dot product with the measurement momentum transfer, respectively. Then, watershed segmentation (see Figure 5(e)) is used to isolate islands and attribute an independent label to them. The next steps involve fitting a plane to the initial population of voxels contributing to each detected facet and scanning the plane along its normal until the surface is reached. Finally, the fit equation is refined at the surface, and one can therefore identify which surface voxel is contributing to a particular facet. Since a plane is fitted to the facet, one can extract also the angle of the facet (its orientation) with the measurement direction. That angle will be in the range $[0^\circ, 90^\circ]$ for the projection from the South Pole, and in the range $[90^\circ, 180^\circ]$ for the projection from the North Pole. Each dataset being different in terms of measurement geometry, reconstructed object size, voxel size, number of facets and surface roughness, there are several parameters that must be provided by the user. The main parameters are the measured Bragg reflection hkl indices, the threshold on the normalized modulus defining the surface, the threshold defining the minimum distance in pixels between two facets in the stereographic projection, and the threshold defining the background intensity to be masked in the stereographic projection. The success of the algorithm depends on the number of voxels belonging to the facet and also on the reconstructed surface roughness. Small facets and rough reconstructed surfaces are generally missed or badly fitted, and these results are filtered out. Note that twin boundaries such as in the case of nanoparticle 4 will also be identified as facets by the algorithm.

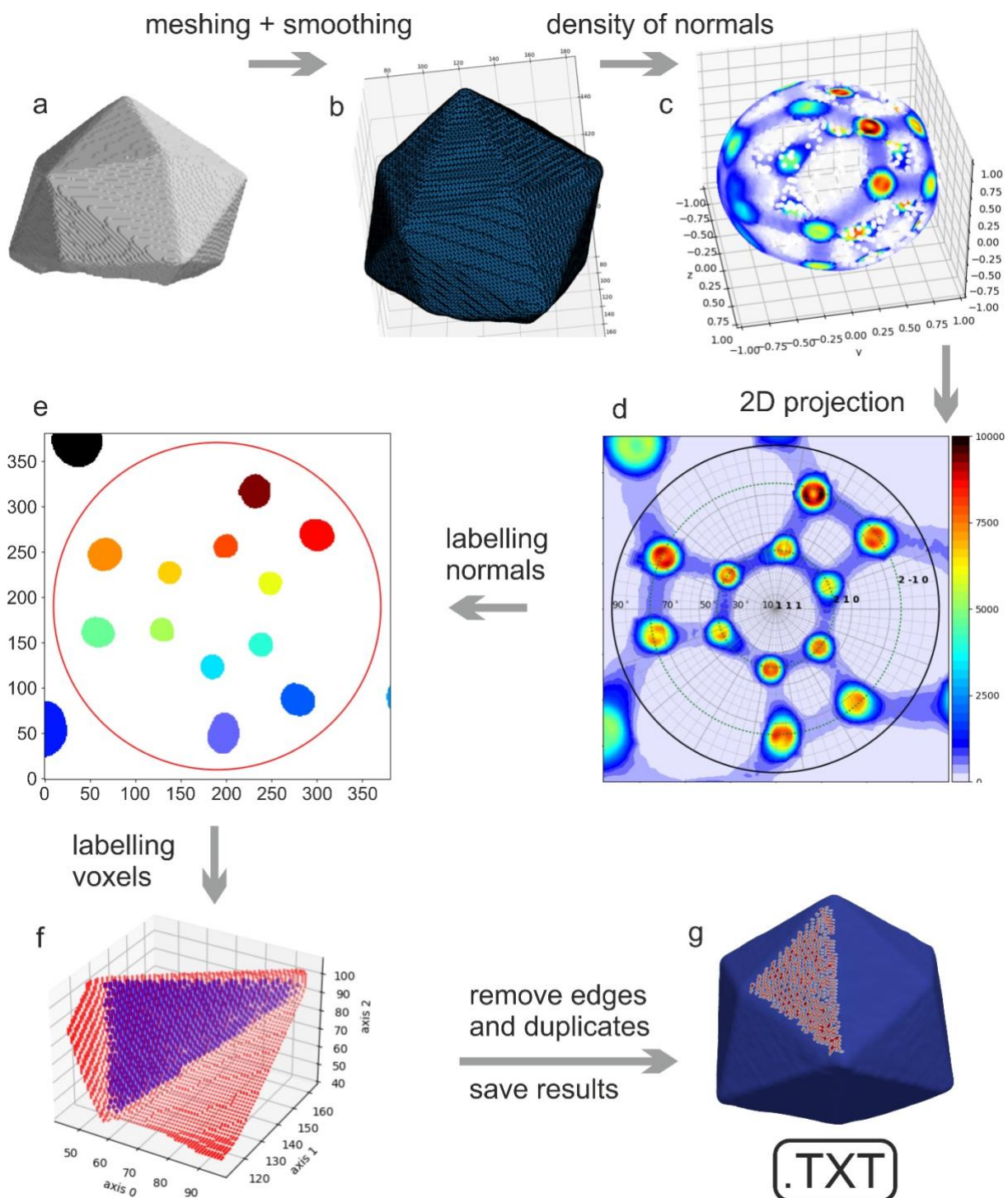


Figure 5. Data workflow of the facet detection algorithm for a nanoparticle reconstructed by phase retrieval, illustrated for THH nanoparticle 1. (a) Reconstructed Bragg electron density. (b) Resulting mesh and smoothing. (c) Weighted normal densities on a sphere. (d) 2D projection of the weighted normal densities. (e) Segmentation and labelling of normal. (f) Identification of the surface voxels. (g) Removal of the voxels from edges and saving of the results.

We applied the automated facet recognition algorithm to the six nanoparticles of Figure 3. The results, sorted by the angle between the facet normals and the measurement direction (Pt **111** or Pt **002**) are presented in **Figure 6**. The error bars indicate the standard deviation of the strain per facets. Nanoparticle 1 yields the best results in terms of the number of detected facets and the fit quality (the facets group in clusters at the expected angle from the measurement direction). Nanoparticle 2 presents a rough facet on its side (see Figure 3). It is convenient to refer to the stereographic projection in order to identify facets that do not belong to the $\{hk0\}$ family. In the case of nanoparticle 2, the facet is very rough as illustrated by the size of the normals density distribution at 90 degrees (see Figure S18) and its centroid corresponds to a $[3\bar{2}\bar{1}]$ facet. In general, more facets are detected in the projection from the South Pole, because they correspond to the facets pointing upwards in the reconstructed nanoparticles, which are large and well defined. Facets pointing down (detected in the projection from the North Pole, at more than 90 degrees of the measurement direction) are often small, rough or absent due to the electrochemical synthesis process onto glassy carbon. The twin boundary of nanoparticle 4 is also crossed by a dislocation, resulting in a large distribution of strain at this interface. Overall, the distribution of strain per facet is relatively small, in the range of $\sim 0.1\%$, and is increased when the shape of the nanoparticle departs from the ideal shape (*e.g.* for nanoparticles 2 and 6) or in the presence of defects (nanoparticle 4). The strain deviation for nanoparticle 6 is large, probably because the nanoparticle is small and imperfect: local strains at edges and corners, and strains due to surface roughness are influencing the retrieved facet strain.

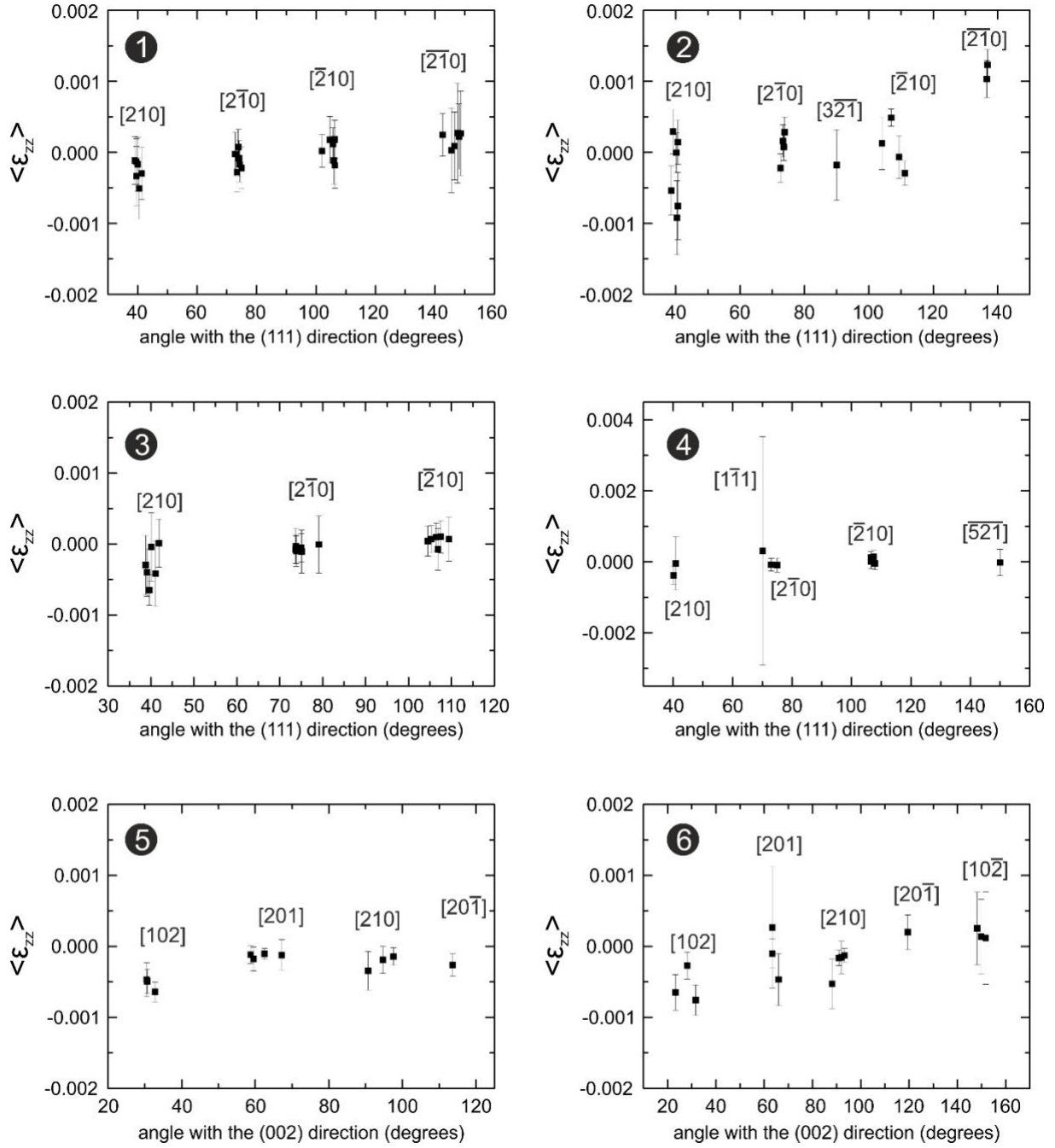


Figure 6. Facet-dependent out-of-plane strain ϵ_{zz} extracted for the six nanoparticles, sorted by angle with the measurement direction. The Miller indices $[hkl]$ of the facets normals are indicated in the plots. Error bars represent the standard deviation.

For a free clean surface it is expected – because of crystallographic symmetry – that the surface strain is the same for all $\langle 102 \rangle$ facets. Due to the measurement geometry, the strain values for $[210]$ facets and $[\bar{2}\bar{1}0]$ facets should be identical for a perfect particle; similarly, $[2\bar{1}0]$ and $[\bar{2}10]$ should also have the same strain. Instead, we observe an increase of the strain

for facets pointing towards the substrate. This difference may arise due to the smaller size of the bottom facets (all particles present a hole in the bottom because of the synthesis process), interactions with the substrate and/or different states of the facet surfaces: adsorb species, roughness, surface reconstructions *etc...*

Since we obtain only one component of the strain in a BCDI measurement, we can compare directly only facets whose normal have the same angle with the measurement direction in Figure 6. In order to ease the interpretation, one can make the assumption that the surface relaxation happens along the facet normal for a perfectly shaped model nanoparticle with extended facets. This assumption will break down for small facets, where the local strains at edges and corners will contribute to the facet strain. Under that assumption, we can estimate the total strain by simply dividing by the cosine squared of the angle between the facet normal and the measurement direction (see Supporting Information).^[35] For the six nanoparticles, we isolated voxels belonging to $\langle 210 \rangle$ facets, applied the geometric correction to the measured strain values and averaged over all voxels. The result is presented in **Figure 7**. The estimated mean strain along $\langle 210 \rangle$ facets is slightly negative. For Pt metallic surfaces, $\langle 210 \rangle$ facets are prone to a rather large inward relaxation of the first planes, despite some discrepancy in the values obtained by theoretical calculations.^[36-38] Since we average over a large number of atomic planes, our observation is in agreement with literature while adsorbates resulting from ambient air might slightly influence the observed strain. For nanoparticles 5 and 6, we excluded from the strain estimation the facets orthogonal to the measurement direction: our measurement is not sensitive to the surface relaxation in this facet geometry and the cosine of the facet's angle with the measurement direction is close to 0, resulting in large error bars.

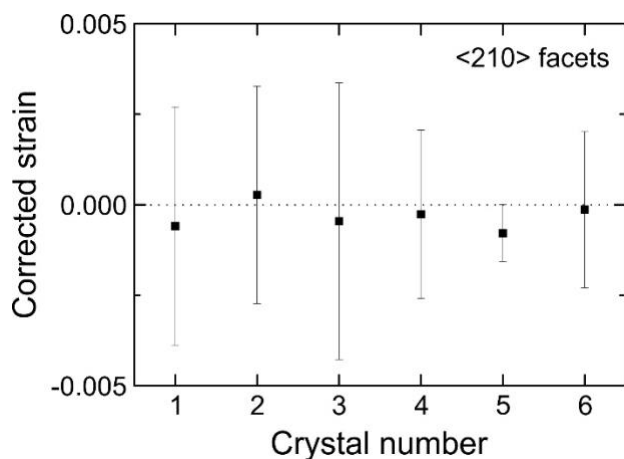


Figure 7. Mean strain for $\langle 210 \rangle$ facets, assuming that the surface relaxation is oriented perpendicular to each facet. The measured strain values have been divided by the cosine squared of the angle between the facet's normal and the measurement direction. Error bars represent the standard deviation. The dotted line a zero strain is a guide for the eye.

It is important to rely on techniques that allow measuring individual nanoparticles as well as providing statistics on the catalytic ensemble. One remaining question is thus related to the statistical relevance of measuring individual nanoparticles in BCDI on the catalytic ensemble, since we would try to establish a good model for catalysis based on a 1-in-a-million particles. BCDI measurements can nowadays be realized on a routine basis within few minutes at third and fourth generation synchrotron sources for particles larger than 50 nm.^[39] Together with advanced analysis methods such as the facet recognition algorithm presented in this study, it is now possible to sample several (tens of) nanoparticles, improve the statistical relevance of the results and reveal heterogeneities in strain, faceting and defects. This allows providing statistics to identify dominant facet characteristics, while also finding deviations from the overall trend. The spatial resolution in BCDI reconstructions to ~ 10 nm still limits the ability to assess the depth-dependent strain in the first atomic layers near the surface, where the variation of the strain is expected to be maximal. For such studies, one has to rely on electron microscopy, at the cost of a loss of 3D information. But note that the strain may propagate from the surface of the crystal into its interior during reaction as demonstrated in Refs. [40-41]. The large penetration depth of X-rays allows more flexibility on the sample environment; as Bragg

coherent X-ray imaging is non-destructive with a proper calibration of the X-ray beam attenuation, it can be applied repeatedly during catalytic reaction on the same nanoparticle. Therefore, it can help understanding strain evolution during reaction using model particles, or in cases with complex in-situ sample environments and nanoparticle mesosizes.

3. Conclusion

We have studied the strain in the surface vicinity of model Pt catalytic nanoparticles. The nanoparticles are in a compressive strain state near the surface. We presented a segmentation method allowing retrieving the average strain values and their standard deviation per facet or family of facets from 3D BCDI datasets. Our study shows that electrochemically synthesized THH nanoparticles show local strains ε_{zz} below 0.1%. The highest strain is observed for particles with defects (twin boundaries or dislocations). This study provides a sound basis for an approach based on model catalytic surfaces, by providing a model system, the characterizing method and data treatment methodologies at the single nanoparticle level. We validate our model system by performing a statistical evaluation of the measured strain on individual facets, in order to extrapolate from the single particle to the ensemble average. Our approach helps developing an understanding of the systematics of structural properties (faceting, defects) in this class of model materials. It opens pathways to investigate *in situ* the internal structural (relationship between strain, shape and complex faceting) evolution of nanoparticles in various gaseous and liquid environments during operation.

Experimental Section/Methods

Sample synthesis

Pt THH particles were synthesized on glassy carbon (GC) electrodes by a square-wave-potential method with a saturated calomel reference electrode (SCE) and a Pt foil counter electrode in 2 mM H_2PtCl_6 and 0.1 M H_2SO_4 electrolyte following the procedure described in

Ref.^[2] The GC electrode is first subjected to a potential of +1.20 V for 2 s to clean the surface and then -0.35 V for 60 ms to create Pt nuclei. The Pt nuclei grow to THH particles by applying a square-wave-potential between +0.04 V and +1.09 V at 100 Hz for 10 min.

Experimental setup details

BCDI measurements were performed at the upgraded ID01 beamline of the ESRF synchrotron.^[17] The required beam size was obtained with a circular Fresnel Zone Plate, which focused the beam. A coherent portion of the beam was selected with high precision slits by matching their horizontal and vertical gaps with the transverse coherence lengths of the beamline: 300 μm (vertically) and 60 μm (horizontally). A circular beam-stop and a circular order-sorting aperture (OSA) were used to block the transmitted beam and higher diffraction orders, respectively. For the wave-front determination, we used a Siemens star in forward geometry with a detector placed 2 m away. The intensity distribution around the **002** or **111** Pt reflections was measured in coplanar diffraction geometry with the sample surface mounted horizontally. The nano-diffraction experiment was performed at beam energy of 9 keV. The diffracted beam was recorded with a 2D MAXIPIX photon-counting detector (516x516 pixels of 55x55 μm^2),^[42] placed at ~0.50 m from the sample for the measurements of the **111** Pt reflections and ~1.26 m for the measurements of the **002** Pt reflections. The detector distances, as well as the rocking angle increments, were chosen in order to ensure oversampling of interferences fringes, depending on the size of the crystal. A typical counting time was 1 s per angle, to get good resolution while preserving the stability of the particle. The sample was mounted on a fast xyz piezoelectric stage with a lateral stroke of 100 μm and a resolution of 2 nm, sitting on a hexapod that was mounted on a (3+2 circles) goniometer.

Phase retrieval

Phase retrieval was carried out on the raw intensity data using PyNX package,^[43,44] imposing that the calculated Fourier intensity of the guessed object agrees with the measured data at each iteration. Defective pixels and gaps in the detector were masked and were not used for imposing the reciprocal space constraint mentioned above. The initial support, which is the constraint in real space, was estimated from the autocorrelation of the diffraction intensity. A series of 1400 RAAR^[45] plus 200 ER^[10,46] was used, including shrinkwrap algorithm^[11] and a correction to account for the partially incoherent incoming wave front.^[47] Mode decomposition^[48] was applied to the best 15 reconstructions out of 500 independent phase retrievals with random phase start. The reconstruction was then corrected for refraction and absorption when the optical path could be estimated (defect-free crystals 1-2-3-6), the small size of the particles ensuring that dynamical diffraction effects could be neglected.^[49] The data was finally interpolated on an orthogonal grid for easier visualization. The resolution of the reconstruction was estimated using the normalized average Phase-Retrieval Transfer Function (PRTF)^[22] at a cutoff value of $1/e$. The PRTF is a measure of how well the retrieved Fourier amplitudes match the square root of the measured diffraction intensity. PRTF for the six nanoparticles are presented in the Supporting Information.

Determination of the isosurface value

The isosurface threshold used to define the surface of the reconstructed object was determined following the method described in Ref.^[30] Given a peaked distribution in the modulus histogram of the reconstructed object, the threshold is defined as the foot of the distribution. Defining a lower threshold results in non-physical strain values, while using a larger threshold results in holes in the reconstructed object. The histograms of the modulus for the six nanoparticles are presented in the Supporting Information. Nanoparticle 5 is a special case: the defective part in the bottom of the nanoparticle is reconstructed with a modulus much smaller than the rest of the crystal, resulting in a double peaked histogram. The analysis of the surface strain (Figures

4, 6 and 7) was realized with a threshold corresponding to the higher peak in the histogram of the reconstructed modulus (see Figure S14).

Facet detection

The facet segmentation algorithm uses similar initial steps as described in Ref.^[32] for the facet detection; the approach for extracting the strain per facet has been developed specially for our purpose. The modulus and the strain arrays resulting from the phase retrieval and post-processing are provided as input as well as the isosurface value defining the surface of the nanocrystal. The analysis can be divided into two main parts, namely facet segmentation and facet fitting: first, one determines independent facets, labels them and gets a first estimate of the equations of planes parallel to them. The second step consists in refining the plane parameters by matching it with the reconstructed nanocrystals surface and isolating the voxels belonging to each facet.

In order to identify and label facets, the modulus is first meshed using Lewiner marching cubes^[50], and then smoothed using Taubin's smoothing.^[51] Each triangle of the mesh is described by its three vertices and one normal, which is weighted by the surface of the triangle. A 3D density map is then created by summing for each normal the neighboring normals weighted by their distance, if they are closer than a certain radius. The initial Taubin smoothing step helps obtaining a density map with high intensity regions corresponding to facets (see Figure 5c).

The next step is to project this 4D data (three Cartesian voxel indices and the density) using a stereographic projection.^[34] It provides two 2D plots corresponding to the projections from the South Pole and North Pole respectively, the measurement direction corresponding to the North Pole. The densities of normals are then inverted (an area of lower intensity corresponding now to a facet), and the user must provide a threshold corresponding to the background density (density corresponding to no facet). New maps of the distance of the remaining density to the

background intensity are calculated. From these distance maps, the local minima are identified, and labels are assigned to them. A parameter defining the minimum distance between two local minima must be provided by the user. Then, watershed segmentation is applied in order to assign a label to each point of the projections (label 0 being the background). A facet orthogonal to the measurement direction will appear in both projections and will result in duplicated labels. Therefore, the duplicity of labels is assessed using the position of the corresponding points on the stereographic projection compared to the circle at 90 degrees from the measurement direction. Now that the facets have been identified uniquely and labelled on the stereographic projections, one can go back to the corresponding normals, mesh vertices and finally voxels using array indices which are preserved during all calculations. Note that these voxels may not correspond anymore exactly to the original object due to smoothing: typically, the smoothed object is slightly smaller than the original one. The voxels identified so far are used as an initial population of voxels belonging to a particular facet (label) in order to estimate the equation of a plane parallel to it.

The first estimate of the plane equation is determined by minimizing the distance of the label's voxels to it. Then, the plane is translated along its normal in order to match it with the surface voxel layer of the nanocrystal, as defined by the isosurface value. The list of surface voxels belonging to the facet is updated using their distance to the plane, and the plane equation further refined. Edges and corners with their low-coordinated atoms may influence the strain statistics of the neighboring facets. Therefore, the crystal edges are isolated using a threshold on their coordination number, and the corresponding voxels are excluded from the list of voxels belonging to the facets (labels).

The analysis script for determination of facet dependent strain is available on public repositories.^[33]

Supporting Information

Supporting Information is available from the Wiley Online Library or from the author.

Acknowledgements

The authors are grateful to ESRF Synchrotron for allocating beamtime. The measurement was performed at beamline ID01. We thank H. Djazouli for his excellent support during the preparation of the experiment, and V. Favre-Nicolin for his continuous improvement of the PyNX package used here for phase retrieval. E. Hensen acknowledges financial support of NWO TOP and KNAW CEP grants. M.-I. Richard acknowledges financial support from ANR Charline (ANR-16-CE07-0028-01) and ANR Tremplin ERC (ANR-18-ERC1-0010-01). This project has received funding from the European Research Council (ERC) under the European Union's Horizon 2020 research and innovation programme (grant agreement No. 818823).

Conflict of Interest

The authors declare no conflict of interest.

Data Availability Statement

The data that support the findings of this study are openly available in the Coherent X-ray Imaging Data Bank at <https://www.cxidb.org/>, reference number ID 182.

Keywords

Bragg coherent X-ray diffraction imaging, platinum tetrahedral nanoparticles, strain, facet segmentation.

Received: ((will be filled in by the editorial staff))

Revised: ((will be filled in by the editorial staff))

Published online: ((will be filled in by the editorial staff))

References

- [1] M., Poliakoff, J. M. Fitzpatrick, T. R. Farren, P. T. Anastas, *Science* **2002**, 297, 807–810.
- [2] N. Tian, Z.-Y. Zhou, S.-G. Sun, Y. Ding, Z. L. Wang, *Science* **2007**, 316, 732–735.

- [3] J. Xiao, S. Liu, N. Tian, Z.-Y. Zhou, H.-X. Liu, B.-B. Xu, S.-G. Sun, *J. Am. Chem. Soc.* **2013**, 135, 18754–18757.
- [4] M. T. M. Koper, *Nanoscale* **2011**, 3, 2054-2073.
- [5] N. Tian, Z.-Y. Zhou, S.-G. Sun, *J. Phys. Chem. C* **2008**, 112, 19801–19817.
- [6] G. A. Somorjai, D. W. Blakely, *Nature* **1975**, 258, 580-583.
- [7] S.-G. Sun, A.-C. Chen, T.-S. Huang, J.-B. Li, Z.-W. Tian, *J. Electroanal. Chem.* **1992**, 340, 213–226.
- [8] F. Yang, D. Deng, X. Pan, Q. Fu, X. Bao, *Natl. Sci. Rev.* **2015**, 2, 183–201.
- [9] B. Ingham, S. C. Hendy, D. D. Fong, P. H. Fuoss, J. A. Eastman, A. Lassesson, K. C. Tee, P.Y. Convers, S. A. Brown, M. P. Ryan, M. F. Toney, *J. Phys. D: Appl. Phys.* **2010**, 43, 075301.
- [10] J. R. Fienup, *Appl. Opt.* **1982**, 21, 2758–2769.
- [11] S. Marchesini, H. He, H. N. Chapman, S. P. Hau-Riege, A. Noy, M. R. Howells, U. Weierstall, J. C. Spence, *Phys. Rev. B* **2003**, 68, 140101.
- [12] A. Diaz, C. Mocuta, J. Stangl, B. Mandl, C. David, J. Vila-Comamala, V. Chamard, T. H. Metzger, G. Bauer, *Phys. Rev. B* **2009**, 79, 125324.
- [13] S. Labat, M.-I. Richard, M. Dupraz, M. Gailhanou, G. Beutier, M. Verdier, F. Mastropietro, T. W. Cornelius, T. U. Schüllli, J. Eymery, O. Thomas, *ACS Nano* **2015**, 9, 9210–9216.
- [14] M. Watari, R. A. McKendry, M. Vöggtli, G. Aeppli, Y.-A. Soh, X. Shi, G. Xiong, X. Huang, R. Harder, I. K. Robinson, *Nat. Mater.* **2011**, 10, 862–866.

- [15] T. Kawaguchi, T. F. Keller, H. Runge, L. Gelisio, C. Seitz, Y. Y. Kim, E. R. Maxey, W. Cha, A. Ulvestad, S. O. Hruszkewycz, R. Harder, I. A. Vartanyants, A. Stierle, H. You, *Phys. Rev. Lett.* **2019**, 123, 246001.
- [16] T. Zhu, E. J. M. Hensen, R. A. van Santen, N. Tian, S.-G. Sun, P. Kaghazchi, T. Jacob, *Phys. Chem. Chem. Phys.* **2013**, 15, 2268–2272.
- [17] S. J. Leake, J. Hilhorst, L. Petit, M.-I. Richard, C. Morawe, R. Barrett, L. Zhang, R. A. Homs-Regajo, V. Favre-Nicolin, P. Boesecke, T. U. Schüllli, *J. Synchrotron Radiat.* **2019**, 26, 571–584.
- [18] S. J. Leake, V. Favre-Nicolin, E. Zatterin, M.-I. Richard, S. Fernandez, G. Chahine, T. Zhou, P. Boesecke, H. Djazouli, T. U. Schüllli, *Materials & Design* **2017**, 119, 470-471.
- [19] G. A. Chahine, M.-I. Richard, R. A. Homs-Regajo, T. N. Tran-Caliste, D. Carbone, V. L. R. Jacques, R. Grifone, P. Boesecke, J. Katzer, I. Costina, H. Djazouli, T. Schroeder, T. U. Schüllli, *J. Appl. Crystallogr.* **2014**, 47, 762–769.
- [20] M. Dupraz, G. Beutier, D. Rodney, D. Mordehai, M. Verdier, *J. Appl. Crystallogr.* **2015**, 48, 621–644.
- [21] W. P. Davey, *Phys. Rev.* **1925**, 25, 753–761.
- [22] H. N. Chapman, A. Barty, S. Marchesini, A. Noy, S. P. Hau-Riege, C. Cui, M. R. Howells, R. Rosen H. He, J. C. H. Spence, U. Weierstall, T. Beetz, C. Jacobsen, D. Shapiro, *J. Opt. Soc. Am. A* **2006**, 23, 1179-1200.
- [23] A. Ulvestad, M. J. Welland, W. Cha, Y. Liu, J. W. Kim, R. Harder, E. Maxey, J. N. Clark, M. J. Highland, H. You, P. Zapol, S. O. Hruszkewycz, G. B. Stephenson, *Nat. Mater.* **2017**, 16, 565–571.

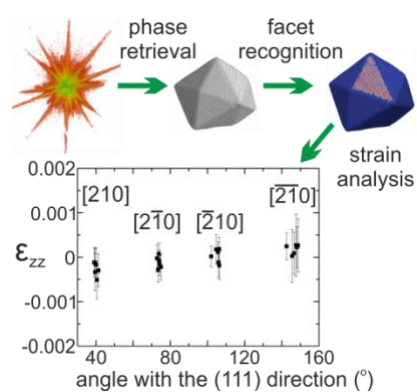
- [24] G. Friedel, (1865-1933) A. du texte. *Leçons de cristallographie* / par G. Friedel,... , **1911**.
- [25] H. Grimmer, W. Bollmann, D. H. Warrington, *Acta Crystallogr., Sect. A: Cryst. Phys., Diffr., Theor. Gen. Crystallogr.* **1974**, 30, 197-207.
- [26] N. Bernstein, E. B. Tadmor, *Phys. Rev. B* **2004**, 69, 094116.
- [27] L. Wang, P. Guan, J. Teng, P. Liu, D. Chen, W. Xie, D. Kong, S. Zhang, T. Zhu, Z. Zhang, E. Ma, M. Chen, X. Han, *Nat. Commun.* **2017**, 8, 2142.
- [28] P. Grammatikopoulos, C. Cassidy, V. Singh, M. Sowwan, *Sci. Rep.* **2014**, 4, 5779.
- [29] J. N. Clark, L. Beitra, G. Xiong, A. Higginbotham, D. M. Fritz, H. T. Lemke, D. Zhu, M. Chollet, G. J. Williams, M. Messerschmidt, B. Abbey, R. J. Harder, A. M. Korsunsky, J. S. Wark, I. K. Robinson, *Science* **2013**, 341, 56-59.
- [30] J. Carnis, L. Gao, S. Labat, Y. Y. Kim, J. P. Hofmann, S. J. Leake, T. U. Schüllli, E. J. M. Hensen, O. Thomas, M.-I. Richard, *Sci. Rep.* **2019**, 9, 17357.
- [31] T. N. Pingel, M. Jørgensen, A. B. Yankovich, H. Grönbeck, E. Olsson, *Nat. Commun.* **2018**, 9, 2722.
- [32] R. Grothausmann, S. Fiechter, R. Beare, G. Lehmann, H. Kropf, G. S. Vinod Kumar, I. Manke, J. Banhart, *Ultramicroscopy* **2012**, 122, 65-75.
- [33] J. Carnis, S. J. Leake. The BCDI Python package can be downloaded from PyPi (<https://pypi.org/project/bcdi/>) or GitHub (<https://github.com/carnisj/bcdi>). DOI: 10.5281/zenodo.3257616, accessed: February, **2021**.
- [34] M.-I. Richard, S. Fernández, J. Eymery, J. P. Hofmann, L. Gao, J. Carnis, S. Labat, V. Favre-Nicolin, E. J. M. Hensen, O. Thomas, T. U. Schüllli, S. J. Leake, *Nanoscale* **2018**, 10, 4833–4840.

- [35] J. F. Nye, *Physical Properties of Crystals: Their Representation by Tensors and Matrices*, Oxford, Clarendon Press, Oxford University Press, 1957.
- [36] X.-G. Zhang, M. A. Van Hove, G. A. Somorjai, P. J. Rous, D. Tobin, A. Gonis, J. M. MacLaren, K. Heinz, M. Michl, H. Lindner, K. Muller, M. Ehsasi, J. H. Block, *Phys. Rev. Lett.* **1991**, 67, 1298-1301.
- [37] A. M. Rodriguez, G. Bozzolo, J. Ferrante, *Surf. Sci.* **1993**, 289, 100-126.
- [38] J. Wan, Y. L. Fan, D. W. Gong, S. G. Shen, X. Q. Fan, *Modell. Simul. Mater. Sci. Eng.* **1999**, 7, 189–206.
- [39] A. Björling, D. Carbone, F. J. Sarabia, S. Hammarberg, J. M. Feliub, J. Solla-Gullón. *J. Synchrotron Rad.* **2019**, 26, 1830–1834.
- [40] D. Kim, M. Chung, J. Carnis, S. Kim, K. Yun, J. Kang, W. Cha, M. J. Cherukara, E. Maxey, R. Harder, K. Sasikumar, S. K. R. S. Sankaranarayanan, A. Zozulya, M. Sprung, D. Riu, H. Kim, *Nat. Commun.* **2018**, 9, 3422.
- [41] A. R. Passos, A. Rochet, L. M. Manente, A. F. Suzana, R. Harder, W. Cha, F. Meneau, *Nat. Commun.* **2020**, 11, 4733.
- [42] C. Ponchut, J. M. Rigal, J. Clément, E. Papillon, A. Homs, S. Petitdemange, *J. Instrum.* **2011**, 6, C01069.
- [43] O. Mandula, M. Elzo Aizarna, J. Eymery, M. Burghammer, V. Favre-Nicolin, *J. Appl. Crystallogr.* **2016** 49, 1842-1848. <http://ftp.esrf.fr/pub/scisoft/PyNX/>, accessed: December, **2020**.
- [44] V. Favre-Nicolin, G. Girard, S. Leake, J. Carnis, Y. Chushkin, J. Kieffer, P. Paleo, M.-I. Richard, *J. Appl. Crystallogr.* **2020**. 53, 1404–1413.

- [45] D. R. Luke, *Inverse Problems* **2005**, 21, 37–50.
- [46] R. Gerchberg, O. Saxton, *Optik* **1972**, 35, 237–246.
- [47] J. N. Clark, X. Huang, R. Harder, I. K. Robinson, *Nat. Commun.* **2012**, 3, 993.
- [48] V. Favre-Nicolin, S. Leake, Y. Chushkin, *Sci. Rep.* **2020**, 10, 2664.
- [49] W. Hu, X. Huang, H. Yan, *J. Appl. Crystallogr.* **2018**, 51, 167-174.
- [50] T. Lewiner, H. Lopes, A. Wilson Vieira, G. Tavares, *J. Graph. Tools* **2003** 8, 1-15.
- [51] G. Taubin, T. Zhang, G. Golub, in *Computer Vision ECCV'96, Lecture Notes in Computer Science*, vol.1064, (Eds: B. Buxton, R. Cipolla), Springer, Berlin, Heidelberg, 1996, pp.283–292.

ToC

We study the uniformity of electrochemically synthesized model catalysts using Bragg Coherent X-ray Diffraction Imaging. We obtain three-dimensional images of several individual nanoparticles, assessing their shape and the specific components of the displacement and strain fields both at the surface and inside. A facet recognition algorithm is applied, which provides facet-dependent structural information for all measured nanoparticles.



Supporting Information

Facet-dependent strain determination in electrochemically synthesized platinum model catalytic nanoparticles.

Jérôme Carnis*, Lu Gao, Sara Fernández, Gilbert Chahine, Tobias U. Schilli, Stéphane Labat, Emiel Hensen, Olivier Thomas, Jan P. Hofmann, and Marie-Ingrid Richard*.

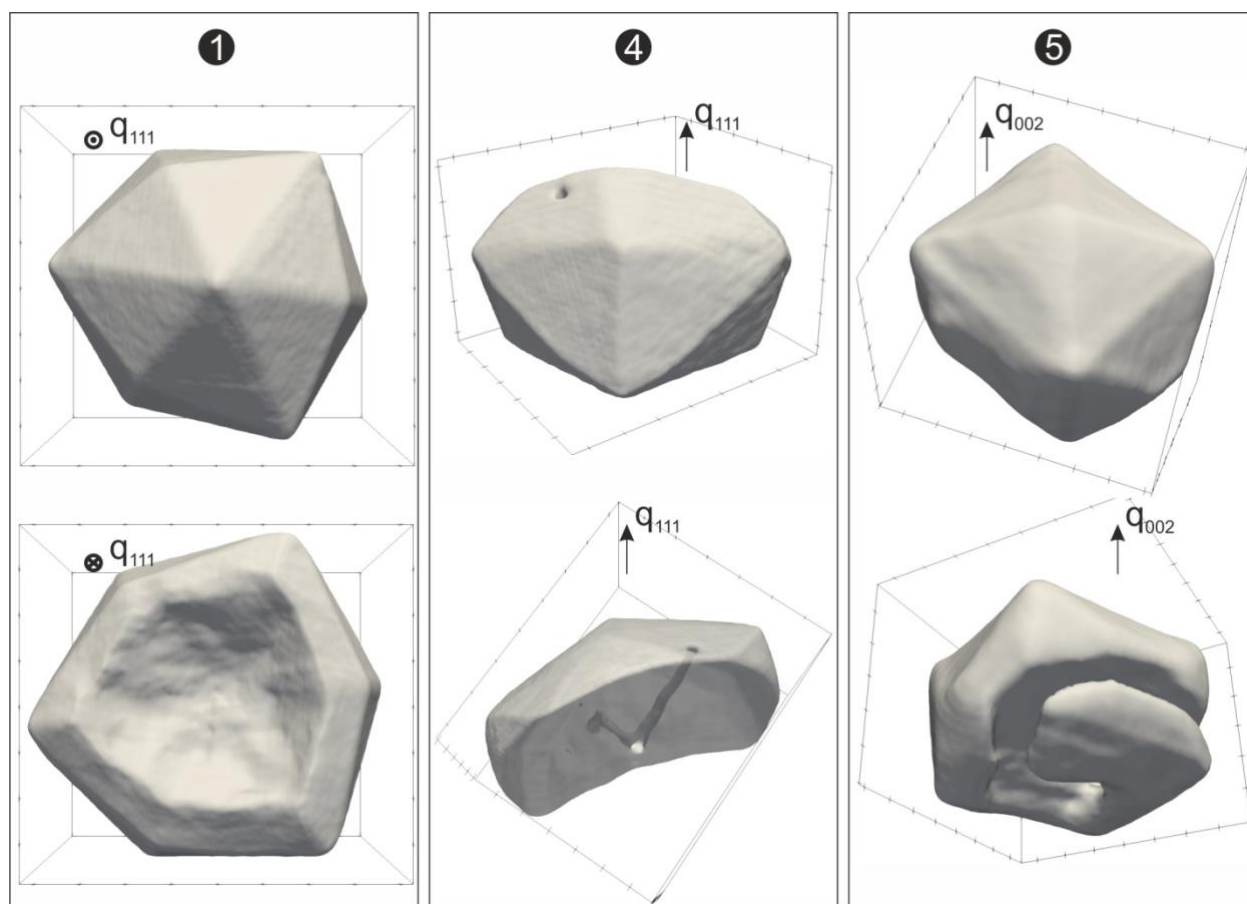


Figure S1. Selected isosurface views of the particles 1, 4 and 5 reconstructed by phase retrieval.

The bottom view of nanoparticle 4 is shown with transparency in order to see the path of the dislocation core through the nanoparticle. The isosurface is determined by a threshold on the reconstructed normalized modulus: 0.38, 0.48 and 0.35, respectively. Ticks represent 50 nm.

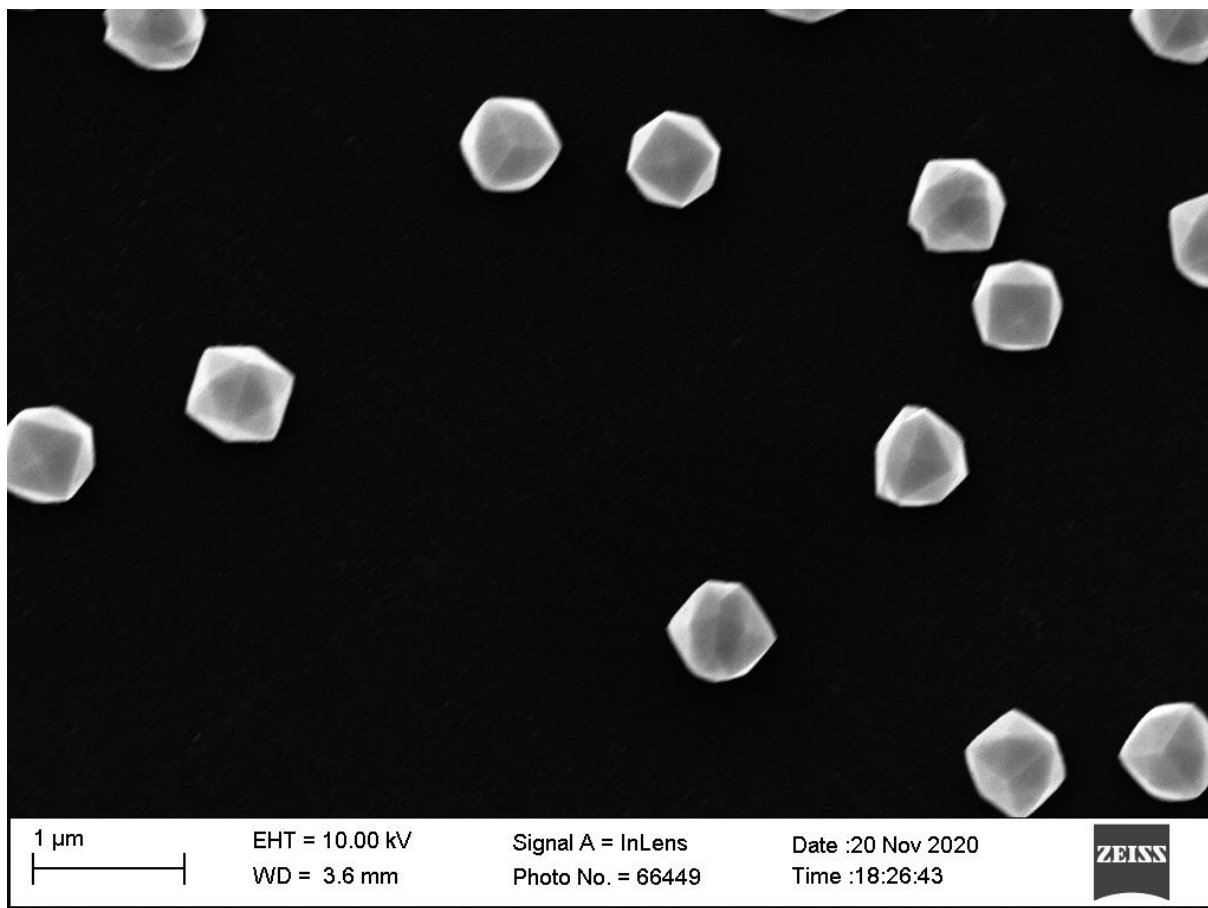


Figure S2. Scanning electron microscopy image of synthesized platinum tetrahedral nanoparticles, revealing twinning for some of the particles.

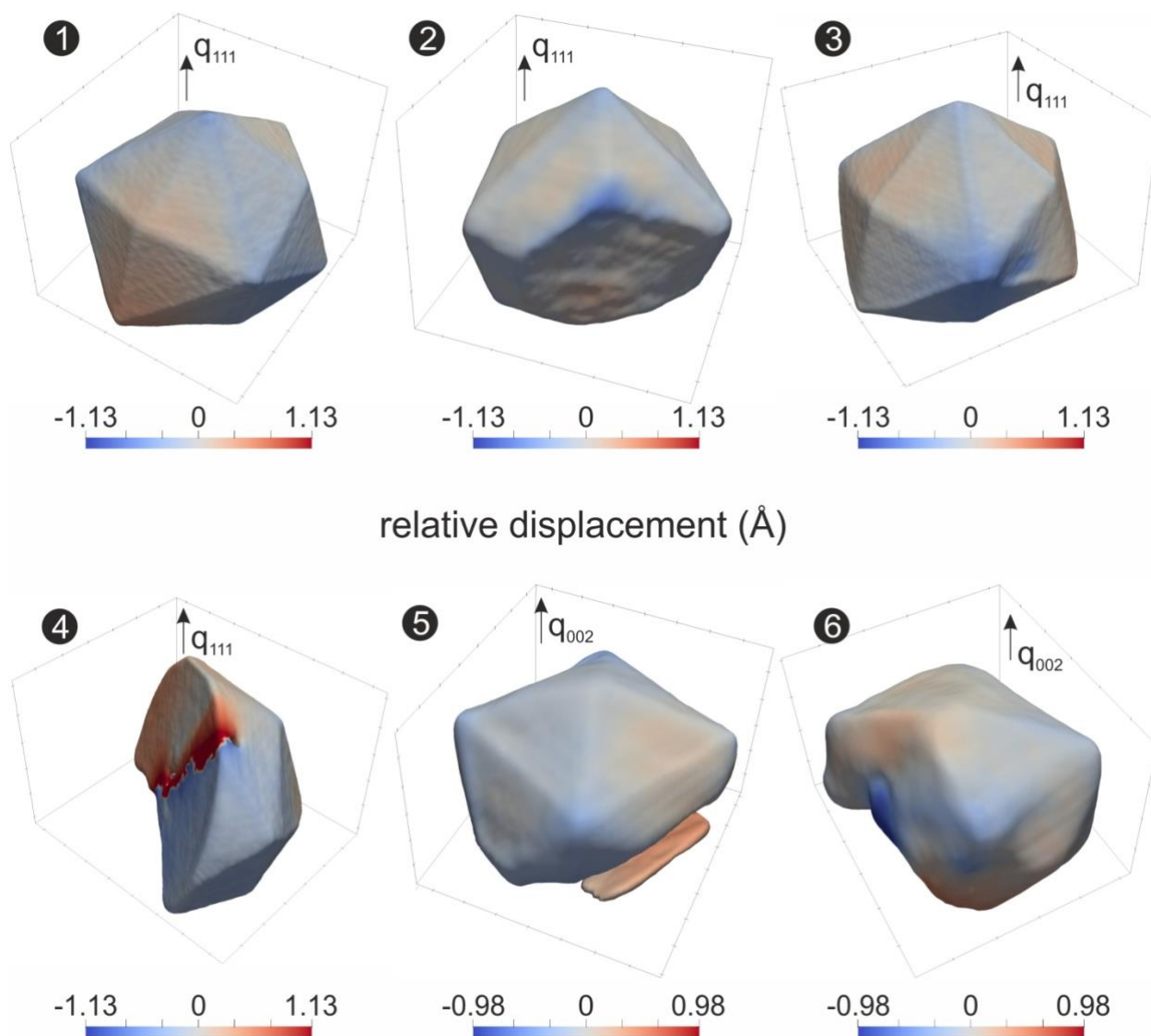


Figure S3. Relative displacement U_z represented on isosurface views of the six different THH nanoparticles reconstructed by phase retrieval. The isosurface is determined by a threshold on the reconstructed normalized modulus: 0.38, 0.48, 0.48, 0.48, 0.35 and 0.25, respectively. The measurement direction has been aligned with the vertical axis of the reconstructed volume. Ticks represent 50 nm.

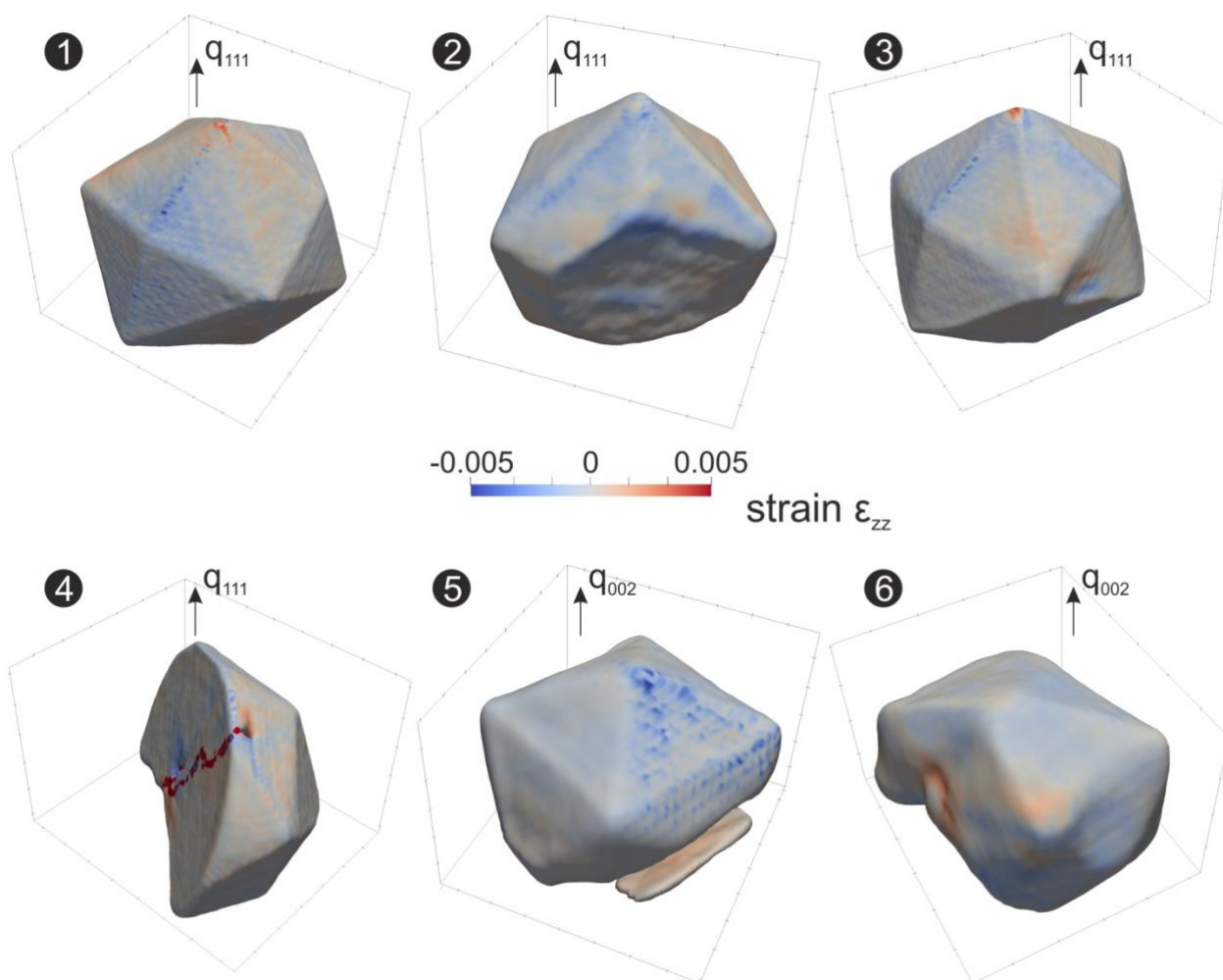


Figure S4. Strain component ϵ_{zz} represented on isosurface views of the six different THH nanoparticles reconstructed by phase retrieval. The isosurface is determined by a threshold on the reconstructed normalized modulus: 0.38, 0.48, 0.48, 0.48, 0.35 and 0.25, respectively. The measurement direction has been aligned with the vertical axis of the reconstructed volume. Ticks represent 50 nm.

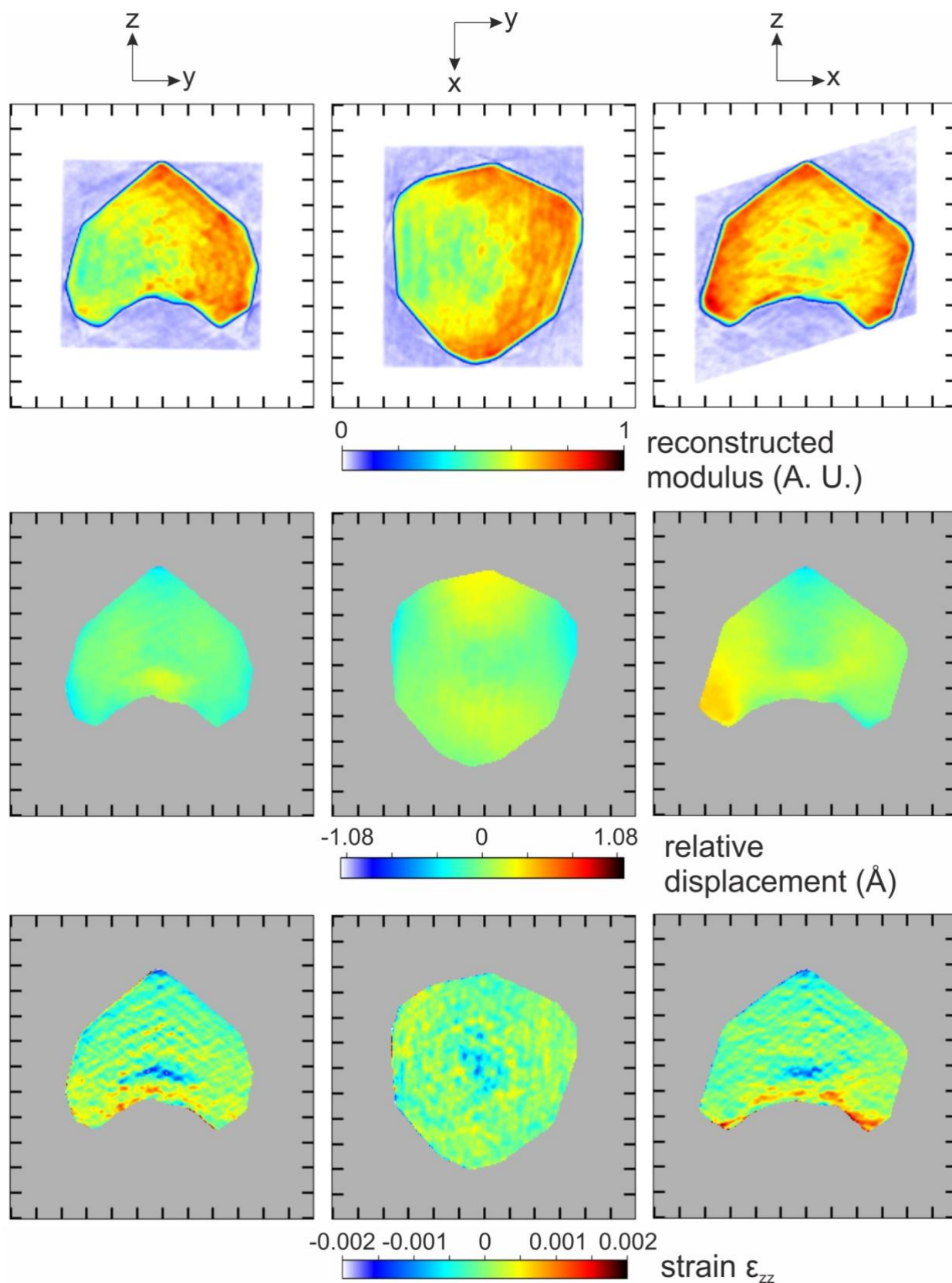


Figure S5. Slices through the reconstructed nanocrystal 1 representing the normalized modulus (first row), the relative displacement U_z (second row) and the strain component ϵ_{zz} (third row).

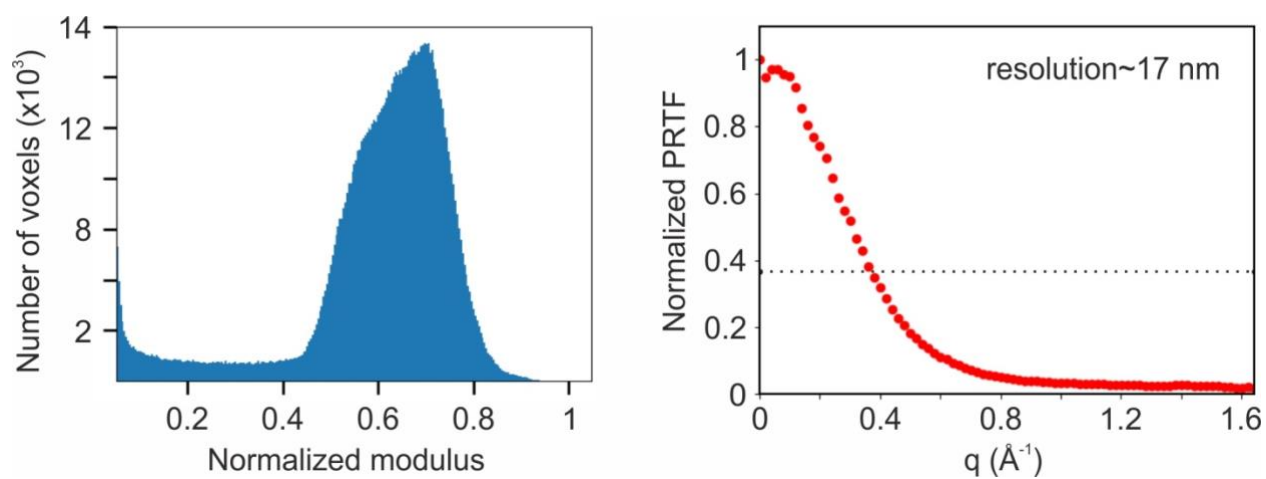


Figure S6. (Left) Histogram of the normalized modulus of the reconstructed nanocrystal 1 and (right) corresponding spherically averaged phase retrieval transfer function. The dashed line corresponds to the value $1/e$ used to estimate the average resolution.

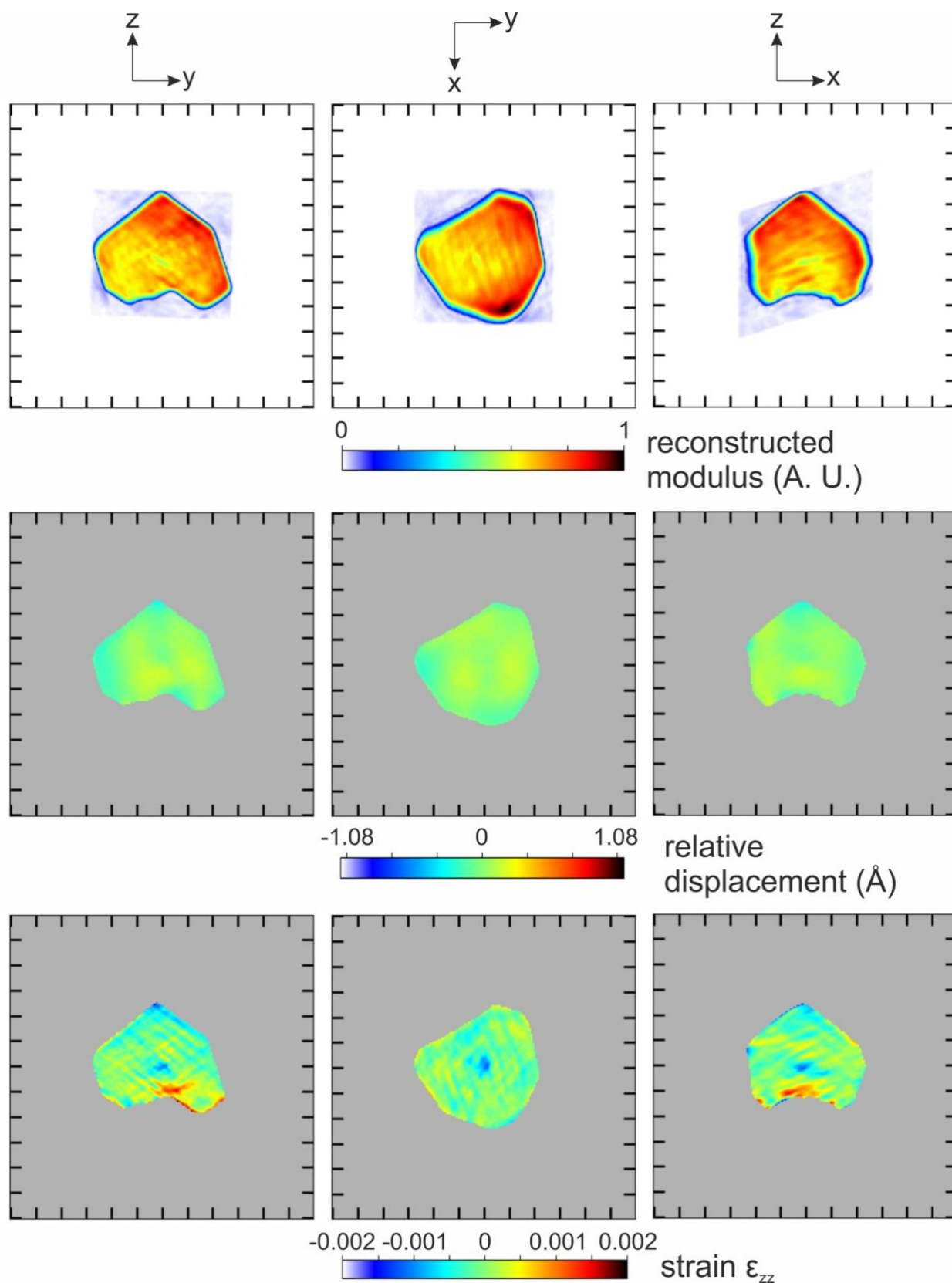


Figure S7. Slices through the reconstructed nanocrystal 2 representing the normalized modulus (first row), the relative displacement U_z (second row) and the strain component ϵ_{zz} (third row).

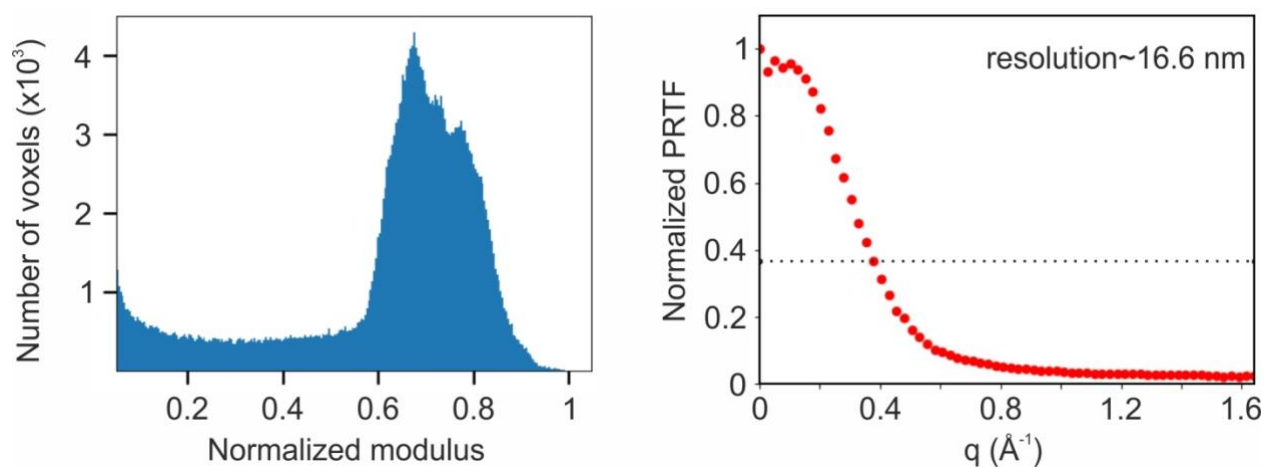


Figure S8. (Left) Histogram of the normalized modulus of the reconstructed nanocrystal 2 and (right) corresponding spherically averaged phase retrieval transfer function. The dashed line corresponds to the value $1/e$ used to estimate the average resolution.

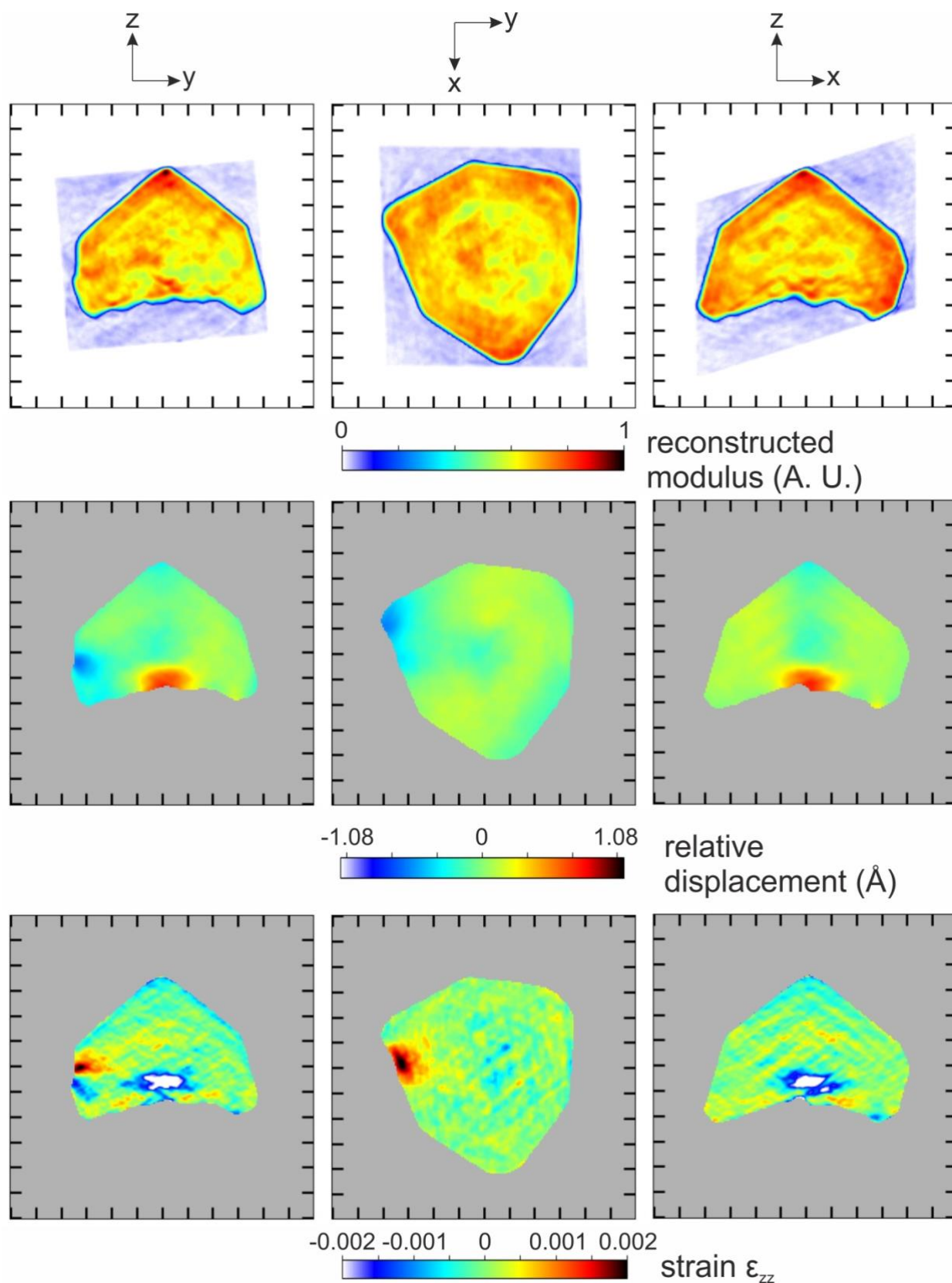


Figure S9. Slices through the reconstructed nanocrystal 3 representing the normalized modulus (first row), the relative displacement U_z (second row) and the strain component ϵ_{zz} (third row).

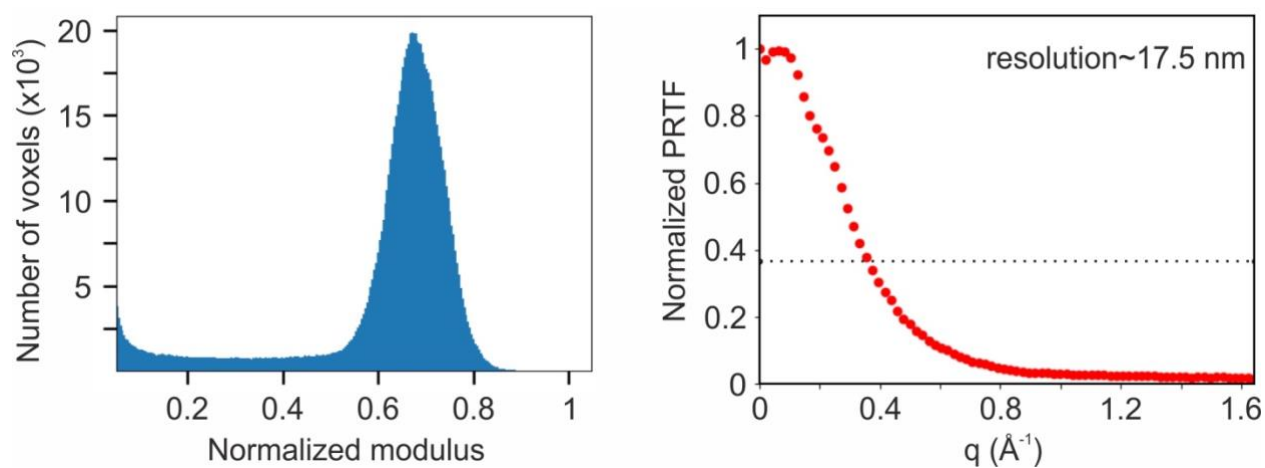


Figure S10. (Left) Histogram of the normalized modulus of the reconstructed nanocrystal 3 and (right) corresponding spherically averaged phase retrieval transfer function. The dashed line corresponds to the value $1/e$ used to estimate the average resolution.

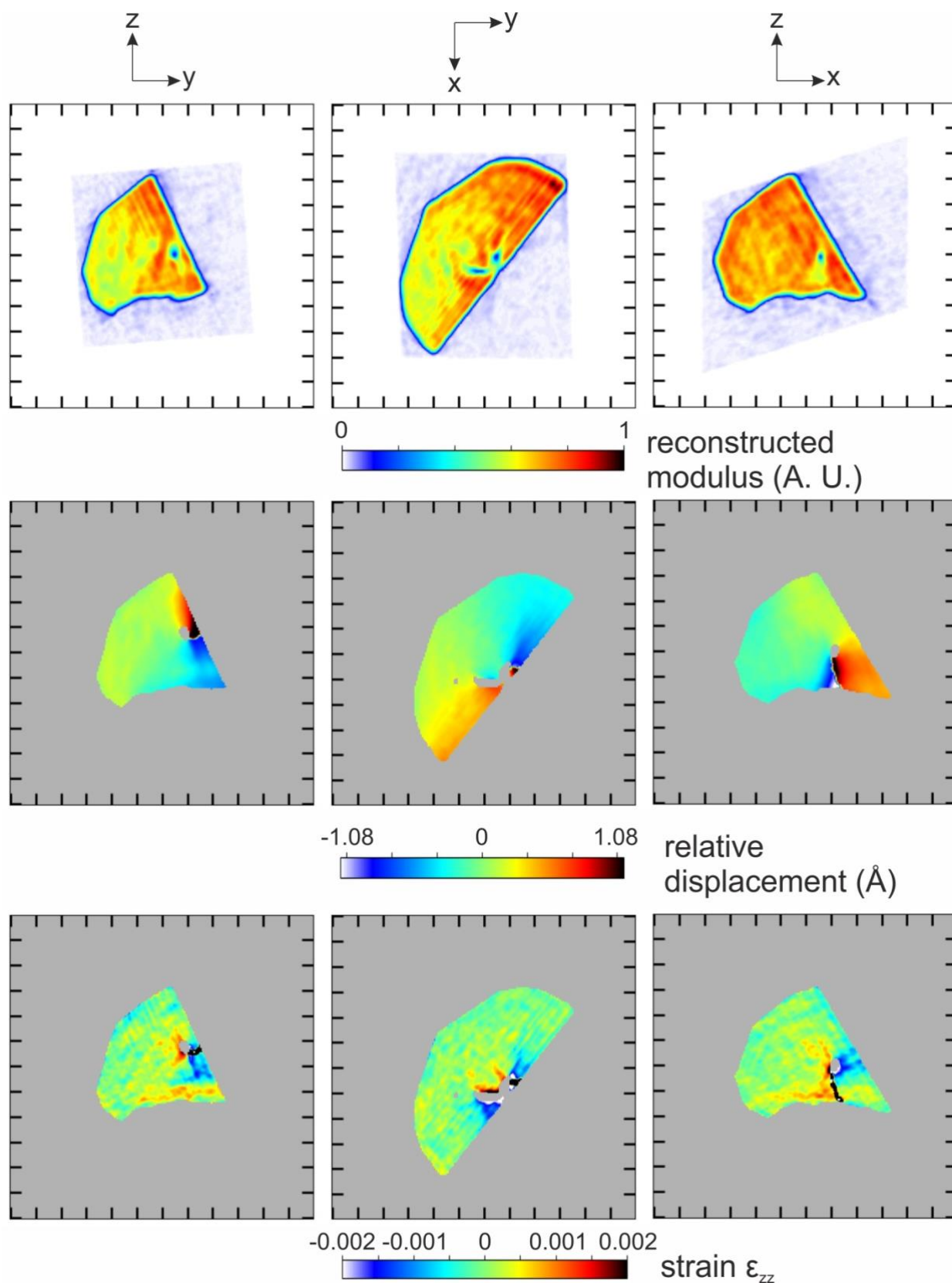


Figure S11. Slices through the reconstructed nanocrystal 4 representing the normalized modulus (first row), the relative displacement U_z (second row) and the strain component ϵ_{zz} (third row).

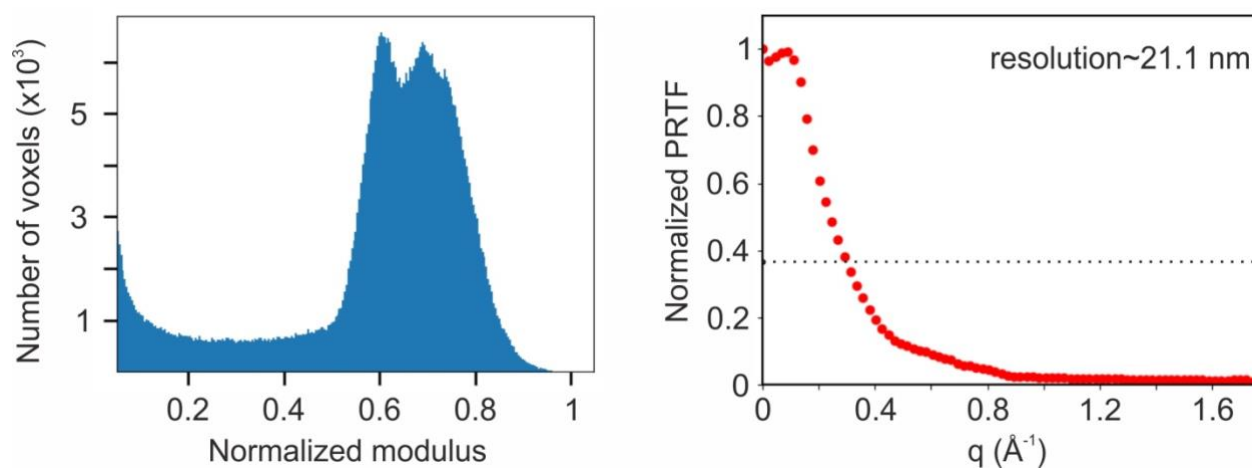


Figure S12. (Left) Histogram of the normalized modulus of the reconstructed nanocrystal 4 and (right) corresponding spherically averaged phase retrieval transfer function. The dashed line corresponds to the value $1/e$ used to estimate the average resolution.

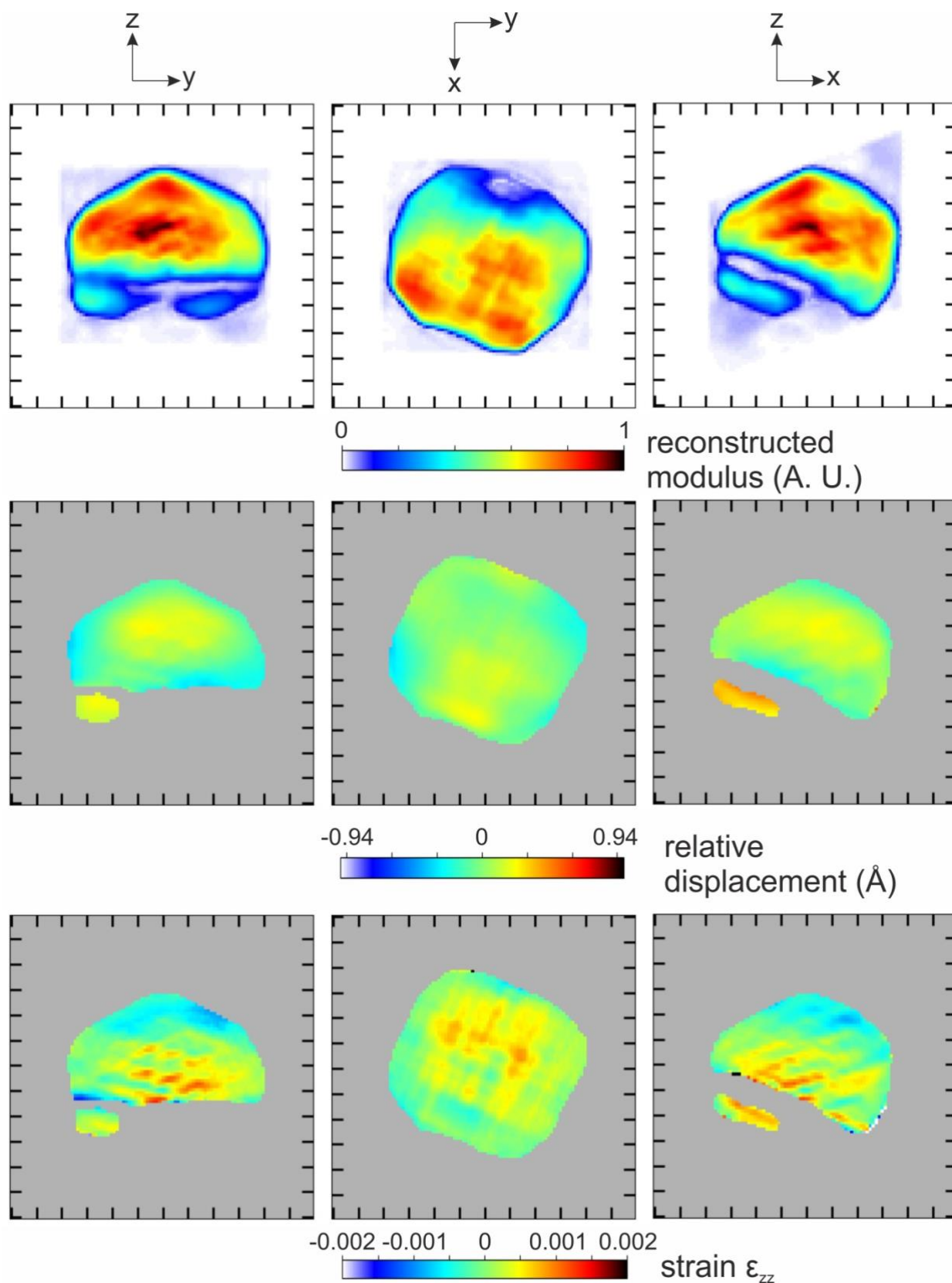


Figure S13. Slices through the reconstructed nanocrystal 5 representing the normalized modulus (first row), the relative displacement U_z (second row) and the strain component ϵ_{zz} (third row).

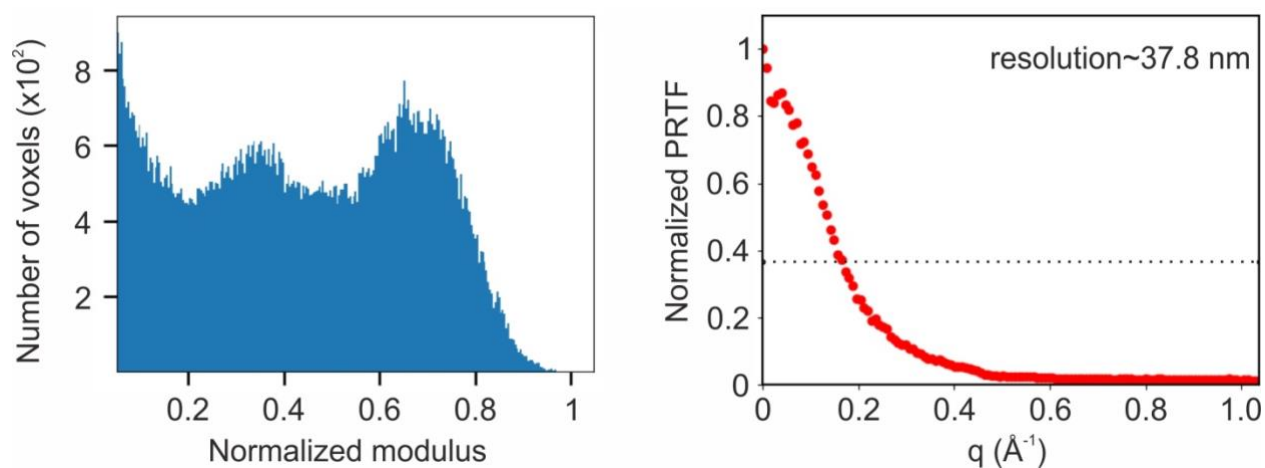


Figure S14. (Left) Histogram of the normalized modulus of the reconstructed nanocrystal 5 and (right) corresponding spherically averaged phase retrieval transfer function. The dashed line corresponds to the value $1/e$ used to estimate the average resolution.

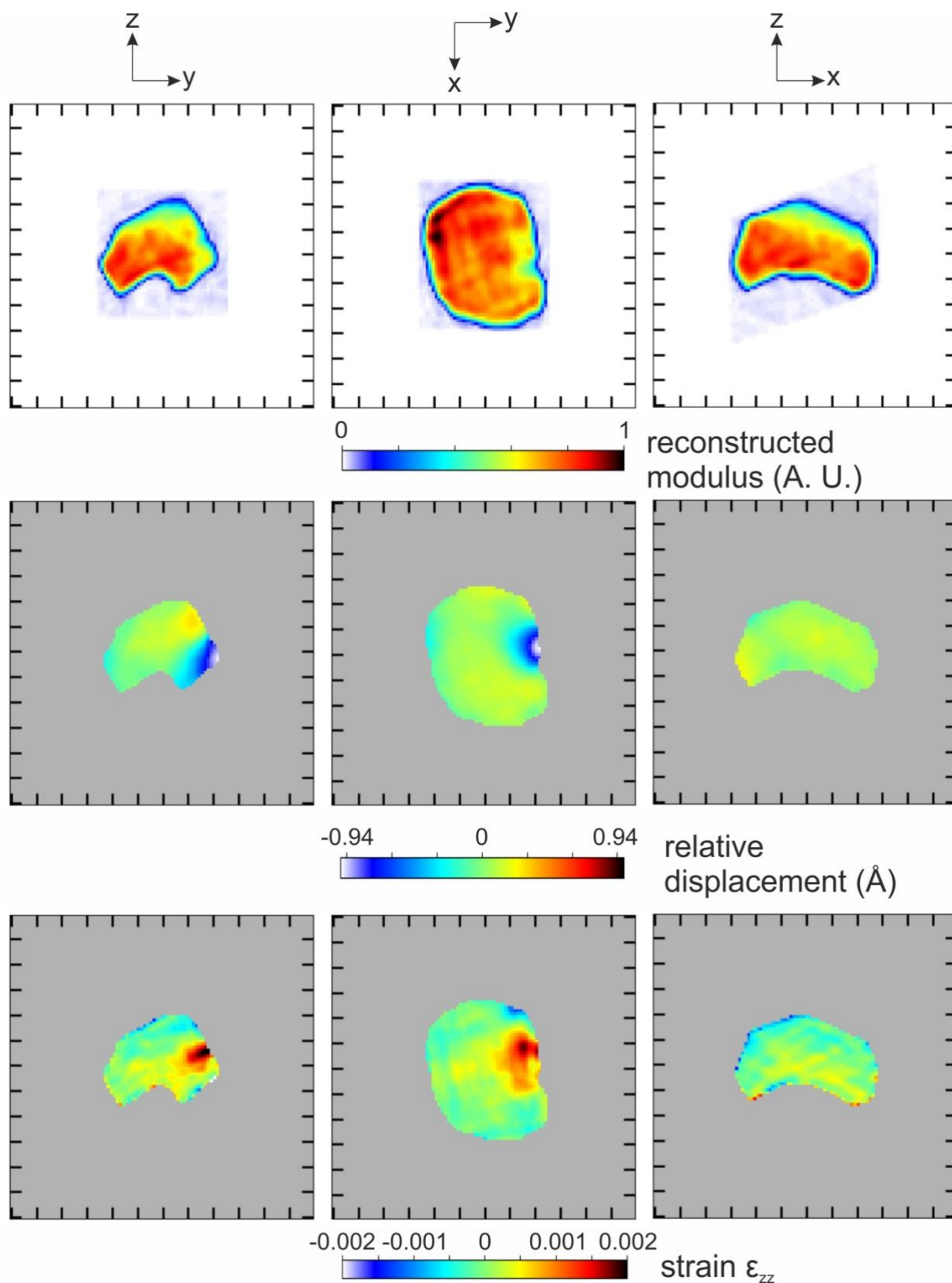


Figure S15. Slices through the reconstructed nanocrystal 6 representing the normalized modulus (first row), the relative displacement U_z (second row) and the strain component ϵ_{zz} (third row).

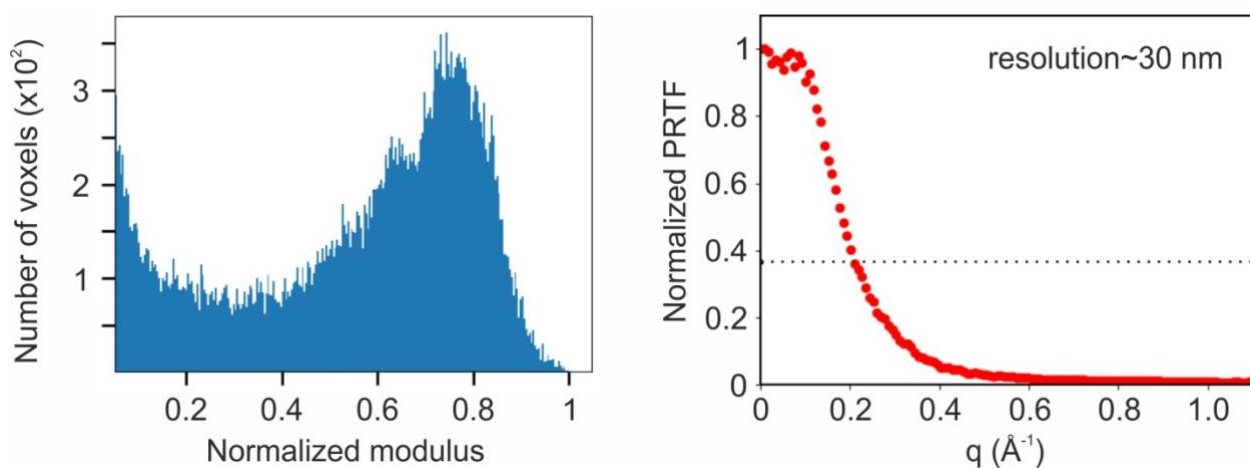


Figure S16. (Left) Histogram of the normalized modulus of the reconstructed nanocrystal 6 and (right) corresponding spherically averaged phase retrieval transfer function. The dashed line corresponds to the value $1/e$ used to estimate the average resolution.

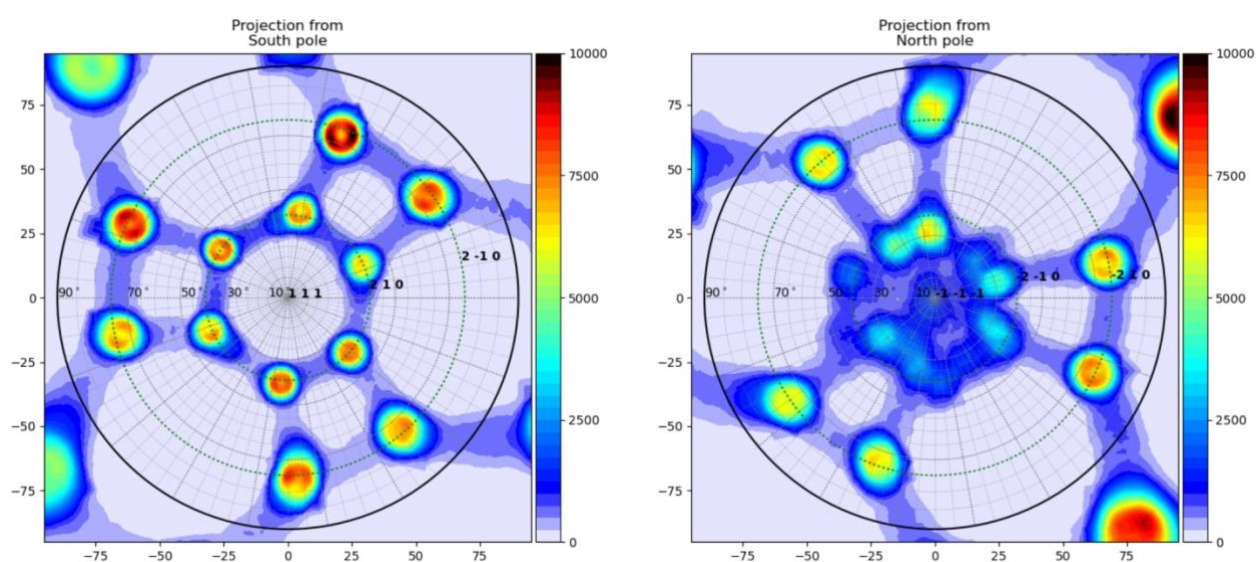


Figure S17. Stereographic projections of the density of normals for the meshed reconstructed nanocrystal 1.

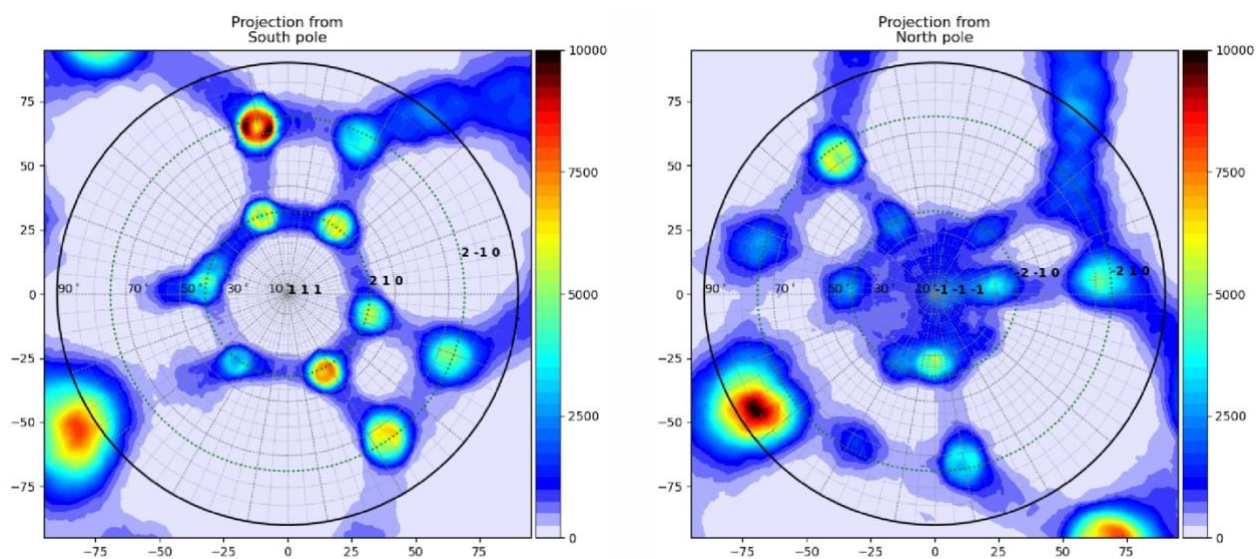


Figure S18. Stereographic projections of the density of normals for the meshed reconstructed nanocrystal 2.

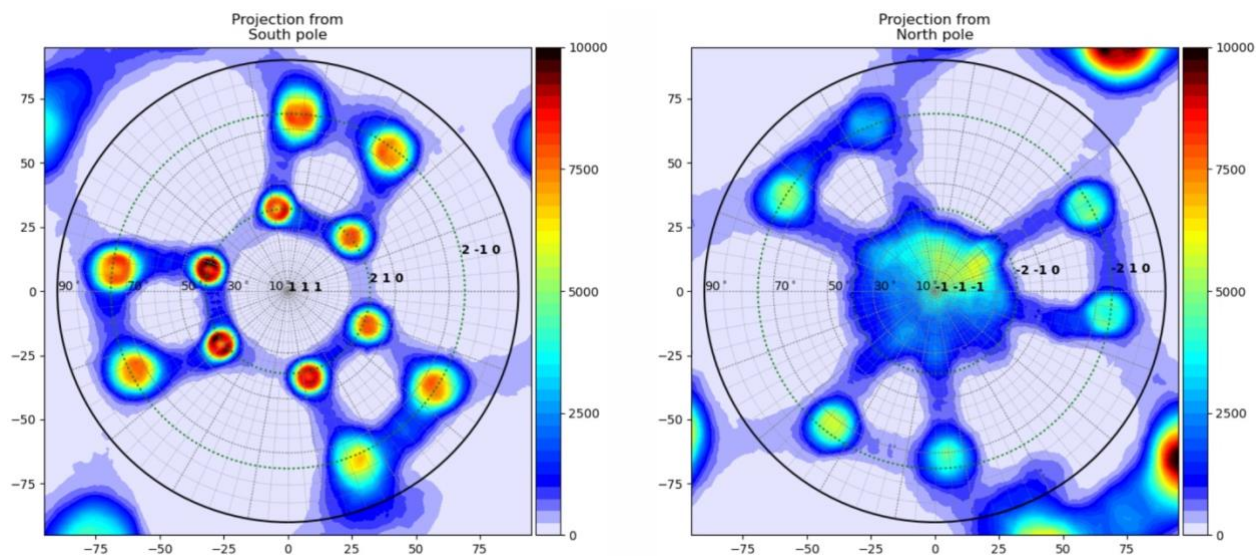


Figure S19. Stereographic projections of the density of normals for the meshed reconstructed nanocrystal 3.

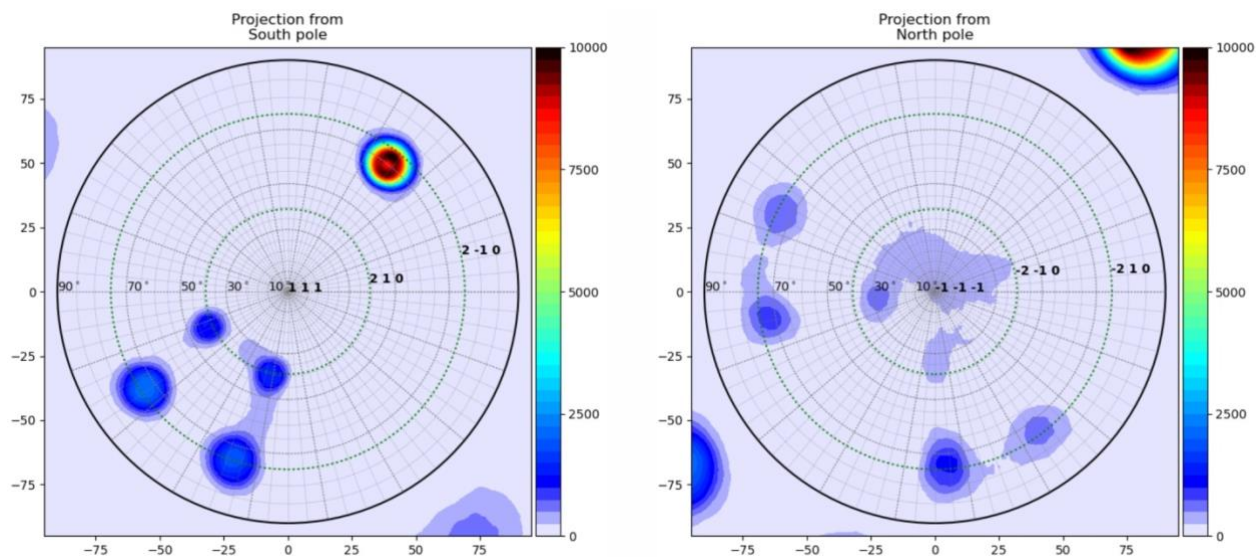


Figure S20. Stereographic projections of the density of normals for the meshed reconstructed nanocrystal 4.

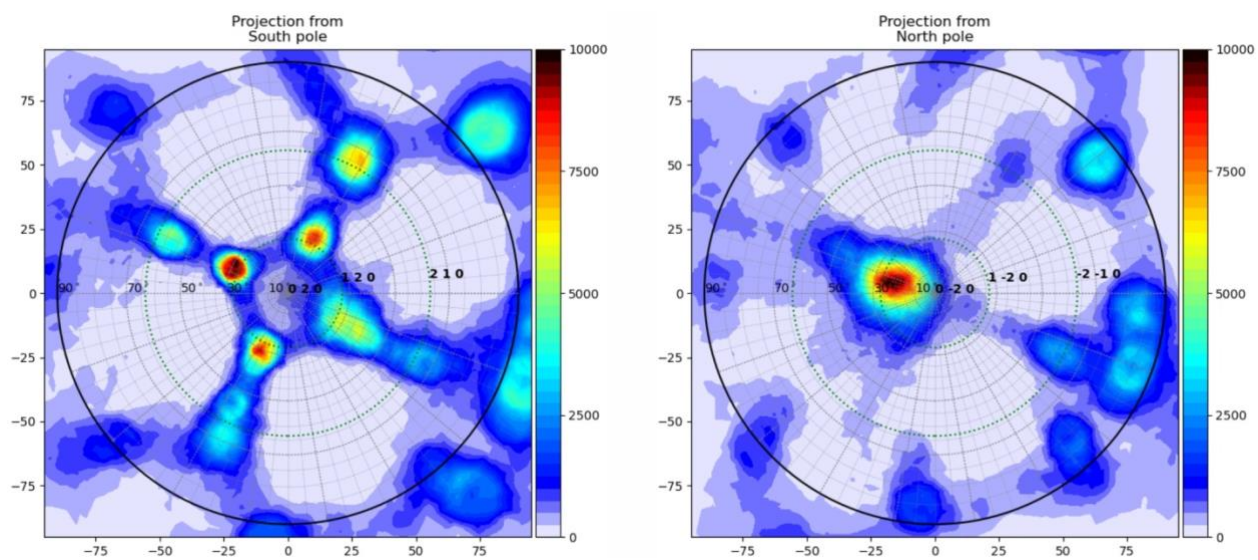


Figure S21. Stereographic projections of the density of normals for the meshed reconstructed nanocrystal 5.

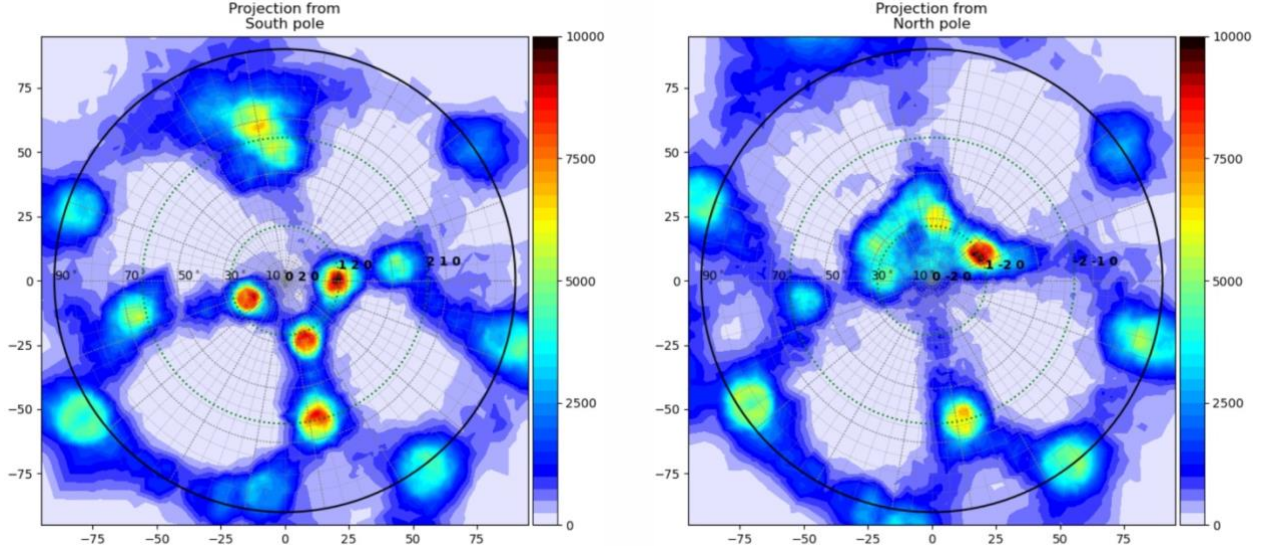


Figure S22. Stereographic projections of the density of normals for the meshed reconstructed nanocrystal 6.

GEOMETRICAL CORRECTION OF THE MEASURED STRAIN:

Let \mathbf{q} be the measurement direction. We define the orthonormal basis $(\mathbf{b1}, \mathbf{b2}, \mathbf{b3})$ such that $\mathbf{b1}$ is orthogonal to \mathbf{q} and is lying in the facet's plane, $\mathbf{b2}$ is orthogonal to $\mathbf{b1}$ and is lying in the facet's plane, $\mathbf{b3}$ is along the facet's normal (see Figure S23). Under the assumption of a surface relaxation along the facet's normal, the local strain tensor can be expressed in the basis $(\mathbf{b1}, \mathbf{b2}, \mathbf{b3})$ as:

$$[\epsilon_{kl}] = \begin{pmatrix} \epsilon_{11} & \epsilon_{12} & \epsilon_{13} \\ \epsilon_{21} = \epsilon_{12} & \epsilon_{22} & \epsilon_{23} \\ \epsilon_{31} = \epsilon_{13} & \epsilon_{32} = \epsilon_{23} & \epsilon_{33} \end{pmatrix} = \begin{pmatrix} 0 & 0 & 0 \\ 0 & 0 & 0 \\ 0 & 0 & \epsilon \end{pmatrix} \quad (1)$$

By construction, $(\mathbf{b1}, \mathbf{b2}, \mathbf{b3})$ are the principal axes of the strain tensor. We define θ as the angle between $\mathbf{b3}$ and \mathbf{q} . We want to transform the components of a symmetrical second-rank tensor from one set of axes to another set which is obtained from the first set by a simple rotation about one of the axes of reference, namely $\mathbf{b1}$.

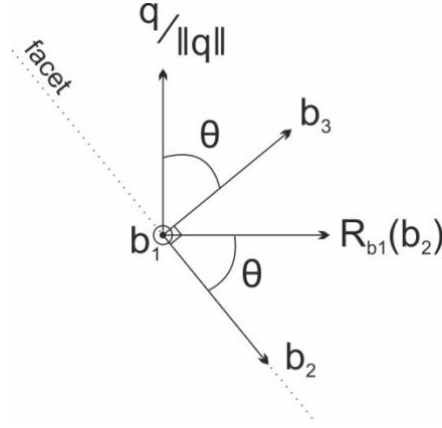


Figure S23. Sketch of the basis used in the calculation of the geometrical correction.

The rotation matrix to consider is:

$$R_{b1} = \begin{pmatrix} a_{11} & a_{12} & a_{13} \\ a_{21} & a_{22} & a_{23} \\ a_{31} & a_{32} & a_{33} \end{pmatrix} = \begin{pmatrix} 1 & 0 & 0 \\ 0 & \cos \theta & \sin \theta \\ 0 & -\sin \theta & \cos \theta \end{pmatrix} \quad (2)$$

The strain components in the new basis ($\mathbf{b}_1, R_{b1}(\mathbf{b}_2), \frac{\mathbf{q}}{\|\mathbf{q}\|}$) are given by (see Ref. S1):

$$\epsilon'_{ij} = a_{ik}a_{jl}\epsilon_{kl} \quad (\epsilon'_{ij} = \epsilon'_{ji}) \quad (3)$$

In equation (3) it will be noticed that k and l are dummy suffixes, while i and j are free. The expansion over k and l gives the equation for each pair of i and j :

$$\begin{aligned} \epsilon'_{ij} = & a_{i1}a_{j1}\epsilon_{11} + a_{i1}a_{j2}\epsilon_{12} + a_{i1}a_{j3}\epsilon_{13} \\ & + a_{i2}a_{j1}\epsilon_{21} + a_{i2}a_{j2}\epsilon_{22} + a_{i2}a_{j3}\epsilon_{23} \\ & + a_{i3}a_{j1}\epsilon_{31} + a_{i3}a_{j2}\epsilon_{32} + a_{i3}a_{j3}\epsilon_{33} \end{aligned} \quad (4)$$

Since only ϵ_{33} is non null due to our choice of basis, the strain tensor in the new basis is:

$$[\epsilon'_{ij}] = \begin{pmatrix} a_{13}a_{13}\epsilon_{33} & a_{13}a_{23}\epsilon_{33} & a_{13}a_{33}\epsilon_{33} \\ a_{23}a_{13}\epsilon_{33} & a_{23}a_{23}\epsilon_{33} & a_{23}a_{33}\epsilon_{33} \\ a_{33}a_{13}\epsilon_{33} & a_{33}a_{23}\epsilon_{33} & a_{33}a_{33}\epsilon_{33} \end{pmatrix} = \epsilon_{33} \begin{pmatrix} 0 & 0 & 0 \\ 0 & \sin^2\theta & \cos\theta \sin\theta \\ 0 & \cos\theta \sin\theta & \cos^2\theta \end{pmatrix} \quad (5)$$

Therefore, under the assumption of a surface relaxation along the facet's normal, the measurement strain value $\epsilon_{zz} = \epsilon'_{33}$ is related to the total strain value $\epsilon = \epsilon_{33}$ by:

$$\epsilon_{zz} = \cos^2\theta \times \epsilon \quad (6)$$

REFERENCES

[S1] J. F. Nye, *Physical Properties of Crystals: Their Representation by Tensors and Matrices*, Oxford, Clarendon Press, Oxford University Press, 1957.